Master Thesis

Characterisation of scintillation light induced by radioactive excitation in the mDOM glass pressure vessel

Supervisor:
Prof. Dr. Alexander Kappes

Second examiner:
Dr. Volker Hannen

A thesis submitted in fulfilment of the requirements for the degree of

Master of Science *at* Westfälische Wilhelms-Universität Münster

by

Markus Dittmer

AG Kappes
Institut für Kernphysik

Münster, April 2020

Declaration of Academic Integrity

I hereby confirm that this thesis on "Characterisation of scintillation light induced by radioactive excitation in the mDOM glass pressure vessel" is solely my own work and that I have used no sources or aids other than the ones stated. All passages in my thesis for which other sources, including electronic media, have been used, be it direct quotes or content references, have been acknowledged as such and the sources cited.

Münster, 17 April 2020 _____

I agree to have my thesis checked in order to rule out potential similarities with other works and to have my thesis stored in a database for this purpose.

Münster, 17 April 2020 _____

"*In the beginning the Universe was created. This has made a lot of people very angry and been widely regarded as a bad move.*"

- Douglas Adams

Contents

Declaration of Academic Integrity **iii**

1 Introduction **1**

2 Neutrino astronomy **3**
2.1 Fundamental properties of neutrinos . . . 3
2.1.1 Interaction . . . 4
2.1.2 Cherenkov radiation . . . 5
2.2 The IceCube neutrino observatory . . . 6
2.2.1 multi-PMT Digital Optical Module (mDOM) . . . 7
2.2.2 IceCube Upgrade . . . 8

3 Photomultiplier tubes **10**
3.1 Photocathode properties and quantum efficiency . . . 11
3.2 Gain and collection efficiency . . . 11
3.3 Pulse timing parameters and pulse types . . . 12
3.4 Uncorrelated background . . . 13
3.5 Single photoelectron spectrum . . . 14

4 Interaction with matter **16**
4.1 Gamma particles . . . 16
4.2 Charged particles . . . 17
4.3 Luminescence . . . 19
4.3.1 Electronic transitions in semiconductors . . . 20
4.3.2 Scintillation yield . . . 22

5 Modelling scintillation **25**

6 Scintillation spectrum **27**
6.1 Measurement setup . . . 27
6.2 Spectrum measurement . . . 28
6.3 Corrections . . . 30

7 Scintillation yield for electrons **34**
7.1 Quantifying scintillation emissions . . . 34
7.1.1 Measurement . . . 34
7.1.2 Afterpulsing-Correction . . . 35
7.1.3 Count loss due to trigger . . . 37
7.1.4 Simulated detection efficiency for different yields . . . 40
7.2 Determining the source activity . . . 43
7.2.1 Gamma spectroscopy . . . 43
7.2.2 Simulation for the detector efficiency . . . 44
7.3 Calculating the electron yield . . . 46
7.4 Impact of lifetimes . . . 48

8 Scintillation yield for alpha particles **52**
8.1 Activity of the alpha source . . . 52
8.2 Determining the alpha yield . . . 54

9 mDOM background simulation **57**

10 Summary and outlook **61**

Acknowledgements **67**

1 Introduction

Ever since the dawn of time it lies within our human nature to gaze upon the sky to look for a purpose and explanation. From ancient Greece, to medieval sailors, up to the first telescope, examining stars has guided us a long way. In this sense, studying the universe provides a powerful source of knowledge for humankind, from which we are able to derive the inherent laws that underlie our cosmos.

In the last century, scientists throughout the world were able to extract deeper information about the universe by expanding the particle observations to more messengers than solely optical photons. The examined signals not only span across the entire electromagnetic spectrum, but furthermore make use of all four fundamental forces and thus the detectors constitute an extensive variety. By combining their data, these detectors yield substantially greater information when studying the same cosmological events and thereby establish the era of multi-messenger astronomy.

One ideal messenger in astroparticle physics is the neutrino. After photons, neutrinos are the most abundant particles in the universe since they are produced in a broad variety of processes. What makes neutrinos even more compelling is that they travel freely in straight paths from their origin due to a low interaction probability. On the flip side, this property causes them to be very difficult to detect. Hence, it is necessary to build enormous detectors for an adequate detection efficiency.

IceCube, currently the largest neutrino observatory with a volume of $\sim 1\,\mathrm{km}^3$, is designed to detect high energy neutrinos from astrophysical sources and is in full operation since the end of 2010 [1]. It is located deep within the Antarctic glacier ice and utilises optical modules for neutrino detection. Since then it was able to detect fluxes of high-energy neutrinos of cosmic origin with energies up to $\mathcal{O}$(PeV) [2]. On September 22$^{\mathrm{nd}}$ 2017, the Fermi and MAGIC gamma ray telescopes followed up an IceCube alert of a high-energy neutrino event and found that it was consistent in direction with the blazar TXS 0506-056. Motivated by this discovery, a search through preceding IceCube data yielded findings of excess emission at the position of the blazar which suggests that blazars are the first identifiable sources of high-energy astrophysical neutrinos [3].
IceCube's successes motivate extensions such as a larger detection volume and improved optical modules amongst other enhancements. One concept is the **m**ulti-PMT **D**igital **O**ptical **M**odule (mDOM) where 24 individual 3" PMTs give an intrinsic angular acceptance, compared to the currently instrumented DOM with a single 10" PMT [4]. The main goals of the first extension - IceCube Upgrade - are world-leading sensitivity to neutrino oscillation physics including tau neutrino appearance as well as improving the calibration of the existing detector which can also be applied to archival data [5]. Progressing, IceCube-Gen2 will consist of $\sim$ 140 additional strings instrumenting $5 - 10\ \mathrm{km}^3$ of ice with the main goal of high-energy neutrino astrophysics [6].

A type of background signal of IceCube is caused by light originating in the modules themselves, consisting of PMTs housed in glass pressure vessels. The investigated *Vitrovex* glass vessels are the baseline components for the mDOM within IceCube Upgrade. This glass contains trace amounts of radioactive isotopes, such as ^{40}K. The respective decays cause background signals via scintillation and Cherenkov photons which are detected by the PMTs subsequently. Since the optical activity of the deep glacier ice is very low, the light produced by the modules themselves represents the dominant background source. In order to fully characterise the expected background of the mDOM and its influence on signal processing, scintillation parameters have to be explored thoroughly. Related studies already investigated Cherenkov light inside the vessels [7], the influence of luminescence in pressure spheres of the AMANDA experiment [8, 9], and the overall influence of α decays on the mDOM performance [10].
This thesis aims to contribute to these findings by investigating characteristics of γ decays, as well as to correct α radiation analyses and their combined effect on the mDOM performance.

2 Neutrino astronomy

This chapter provides a brief introduction to the underlying properties of neutrinos and afterwards presents the detection principles in high-energy ranges used in the IceCube observatory.

2.1 Fundamental properties of neutrinos

Neutrinos are elementary particles that interact rather infrequently with matter. By the second, billions of neutrinos pass the human body whereas only a few interactions are expected to occur within a lifetime.
The Standard Model of particle physics (fig. 2.1) is divided into three classes: Gauge bosons which are the interaction force carriers for the four fundamental forces, quarks, the building blocks of hadrons and baryons, and lastly leptons. Fermions (quarks and leptons) additionally come with an antiparticle each and are further branched into three groups of matter. The electron e, muon μ, and tauon τ form the base of the lepton class. These charged particles are accompanied by neutral counterparts – the neutrinos – which come in three different **flavours** (ν_e, ν_μ, ν_τ) corresponding to their charged counterparts. Due to their lack of charge, these particles only interact weakly or gravitationally. Given the extremely low mass of neutrinos (with an upper boundary of $1.1\,\mathrm{eV/c^2}$ [12]), the latter is negligible, solely leaving weak interactions for this particle.

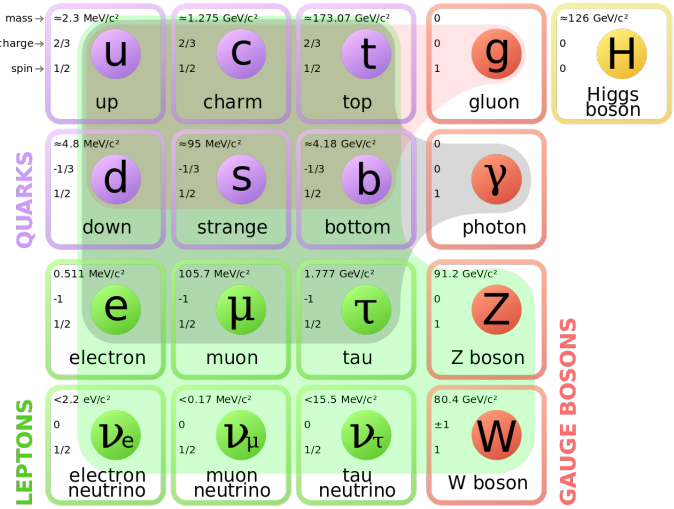

Fig. 2.1: The Standard Model of elementary particles and gauge bosons. Coloured backgrounds illustrate fundamental interactions (red: strong, blue: electromagnetic, green: weak) to the respective mediators. Figure taken from [11].

Neutrino oscillation is the observed periodical conversion of neutrino lepton flavours, meaning that it is not conserved and partially changes after propagation in vacuum or matter. This effect was first observed by the Homestake experiment in the 1960s and later by Kamiokande-II in 1987 [13, 14]. This constitutes that neutrinos cannot be massless as formerly postulated. In fact, description within the Standard Model poses a theoretical problem since the lack of conservation of the lepton number requires additional (interaction) particles.

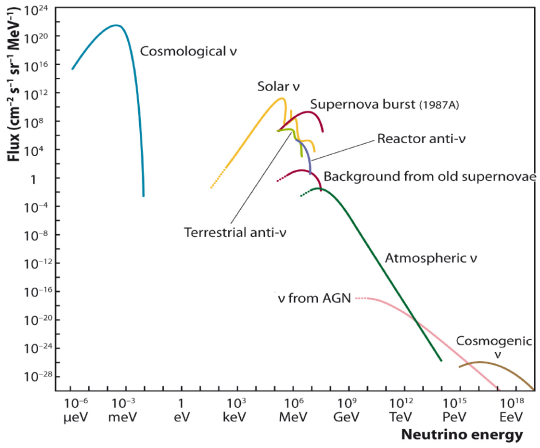

Fig. 2.2: Energy of natural and reactor neutrinos plotted against measured and expected fluxes. Large Cherenkov telescopes perform in the energy range from tens of GeV to hundreds of PeV which have fluxes of immensely lower magnitude than cosmological neutrinos. Figure taken from [15].

High energetic cosmic neutrinos are of particular interest for astroparticle physics since they not only originate from an immense variety of processes but further travel in straight paths from their source due to the virtual lack of interaction, making them the ideal cosmic messenger when searching for cosmic accelerators.
The earth is constantly exposed to bombardment by charged particles dubbed **cosmic rays** which span energy ranges from $\sim 10\,\mathrm{GeV}$ up to $\mathcal{O}(\mathrm{EeV})$ [16]. Promising candidates to be the cause of these high energy particles are SuperNova Remnants (SNR). The subsequent acceleration of cosmic rays following the detonation of supernovae poses the main galactic source of cosmic rays. Particles with even higher energies are considered to be extragalactical, accelerated by Active Galactic Nuclei (AGN) i.e. supermassive black holes. These feature two opposing jets perpendicular to the accretion disk containing extraordinarily relativistic matter, accelerating particles to immense energies [17].
Neutrinos are a by-product of interactions from cosmic rays and are produced either at the acceleration sites or during their propagation. The energy of neutrinos originating from different galactic sources is shown in fig. 2.2 in respect to their respective flux.

2.1.1 Interaction

If a neutrino interacts, it produces charged secondary particles in weak interaction channels with the corresponding gauge bosons Z^0 or $\mathrm{W}^\pm$. The interaction through the former boson is described as **neutral current** (NC) and the latter as **charged current** (CC). The kind of interaction is dependent on the neutrino flavor as well as the energy, whereas the interaction partner adds further variety to the final outcome.
At neutrino energies above 10 GeV, which is the lowest energy domain that large neutrino observatories operate in, interactions are dominated by **deep inelastic scattering** with the constituent quarks of matter. This is described by the reactions

$$\nu_l + N \xrightarrow{Z^0} l + X \quad \text{(CC)} \qquad \text{or} \qquad \nu_l + N \xrightarrow{W^\pm} \nu_l + X \quad \text{(NC)} \tag{2.1}$$

where ν_l represents an (anti)neutrino with the lepton flavour $l \in (e, \mu, \tau)$, N is a nucleon (proton or neutron), and X denotes further products of the interaction as in hadronic particles (potentially an entire hadronic cascade).

The corresponding Feynman diagrams for all four possible interactions are illustrated in fig. 2.3, whereas the subsequent outcome within the detector of the different events are distinguished by tracks or showers.

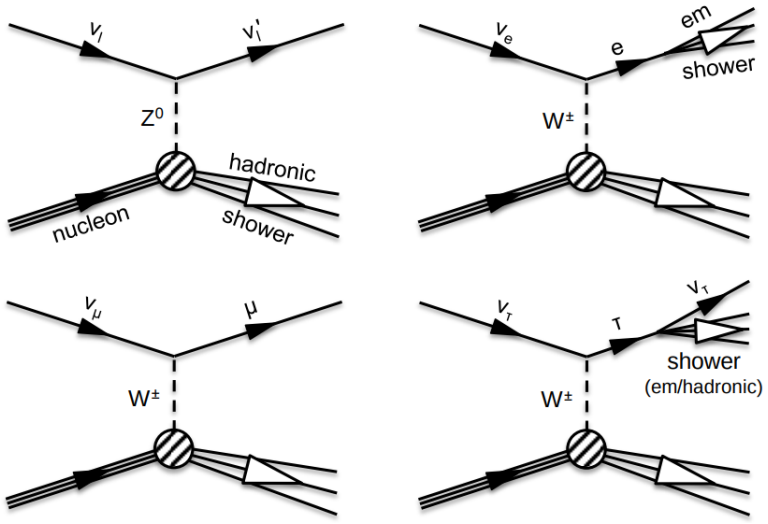

Fig. 2.3: Feynman diagrams for possible neutrino interactions. (Top left) NC interaction for all three flavours l which cause a hadronic shower. (Top right) CC interaction for ν_e result in an electromagnetic shower. (Bottom left) CC interaction for ν_μ where a muon is the outcome. (Bottom right) CC interaction for ν_τ where a shower and a tauon are the product. Figure taken from [18].

2.1.2 Cherenkov radiation

The most common method of indirect detection of neutrinos is utilising Cherenkov radiation. This approach is employed in a variety of neutrino detectors such as ANTARES, KM3NeT and IceCube.
After a charged current interaction (see eq. 2.1), most of the neutrino energy is transferred to the lepton. At high energies this causes the charged particle to travel practically at light speed c_0. Since a transparent interaction medium is necessary for this type of detector, the resulting particle will travel faster than the light speed within the medium $c_n = \frac{c_0}{n}$, where n denotes the refraction index of the interaction medium.

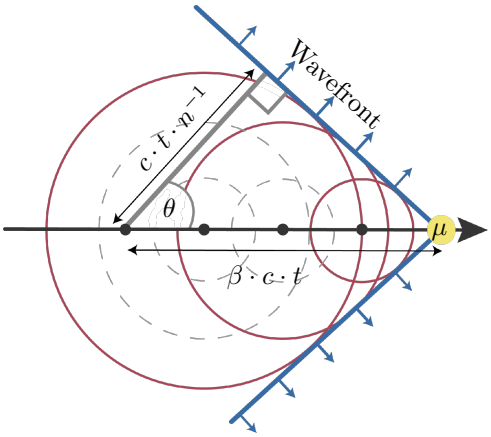

Fig. 2.4: Illustration of the emission of Cherenkov radiation caused by a high energy muon. Figure taken from [10].

If a charged particle travels through a dielectric medium faster than its phase velocity of light, the medium will emit a light signature.[1] The electric field of charged particles polarises the medium by displacing electrons which will return to their original position disposing the excess energy via photons. Under ordinary circumstances, these radiations will interfere destructively and thus exert no relevant signature. In case of particle velocities faster than the speed of light within a medium, wavelets will interfere constructively within wavefronts, thus causing a coherent emission of photons. This process is called Cherenkov radiation and is illustrated in fig. 2.4. These photons are then most commonly detected by optical modules that house Photomultiplier Tubes (PMTs).

[1] The emission spectrum and number of photons radiated per length unit can be determined by the Frank-Tamm formula.

Further, the radiated photons are released in a cone-shaped fashion relative to the path of the travelling charged particle. Since the wavefronts move with $c_n = \frac{c}{n}$ and the particle with $v_p = \beta c$, the opening angle of the cone is given by

$$\cos(\theta) = \frac{cn^{-1}}{\beta c} = \frac{1}{n\beta} = \frac{c_0}{nv_p}. \tag{2.2}$$

2.2 The IceCube neutrino observatory

Since the cross section of neutrinos is considerably small, large detection volumes are required in order to increase the probability of neutrino interactions within the detector medium. Additionally, the flux of astronomical neutrinos reduces significantly towards higher energies, which further reduces the possibility of observed interactions.
Currently, the largest detector in the world with a volume of $1\,\mathrm{km}^3$ is the IceCube neutrino observatory. It is located 1450 m deep within the glacier ice of the South Pole and accommodates a total of 5160 digital optical modules (DOMs) in order to detect Cherenkov radiation produced after neutrinos interact. An illustration of the entire detector is shown in fig. 2.5.

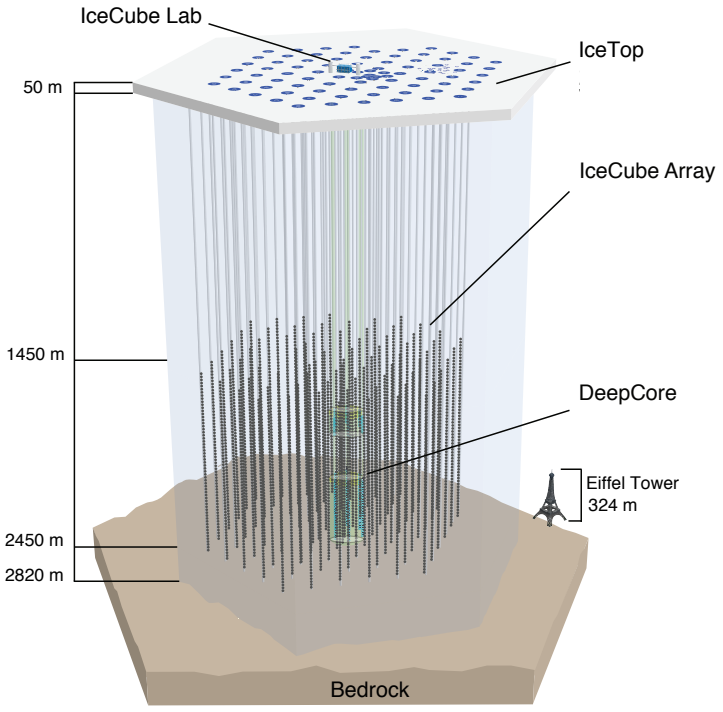

Fig. 2.5: Schematic of the IceCube observatory at the South Pole. Courtesy of the IceCube Collaboration.

The optical modules are deployed on a total of 86 vertical strings of 1 km length, spanning a surface area of $1\,\mathrm{km}^2$. On each string 60 optical modules are mounted with a vertical inter-module separation of 17 m, whereas the collective strings are instrumented in a hexagonal array-like manner with an inter-string distance of 125 m. This span allows for neutrino detection with energy between 100 GeV and $\mathcal{O}$(PeV) [19].
For lower energies on the order of tens of GeV, *DeepCore* is more densely instrumented in the centre of the detector with an average inter-module spacing of 7 m and inter-string distance of 72 m for 8 deployed strings.
At the surface, one can find *IceTop* consisting of water tanks including 2 DOMs each, spanning $1\,\mathrm{km}^2$ of surface area above the strings, forming an air shower detector. IceTop may also serve as a veto for events - thus sorting out atmospheric neutrinos, neutrinos originating from air showers, and muon tracks below a certain energy threshold.
When a neutrino interaction with sufficient energy occurs, whereby Cherenkov light is emitted within the detector, each module signal is sent into the IceCube Laboratory

where data storage and assessment takes place. The amount of Cherenkov light is determined by the neutrino energy, whereas the shape of light signature itself is dependent on the neutrino flavour.

2.2.1 multi-PMT Digital Optical Module (mDOM)

It is evident that the precision of the detector is considerably dependent on the performance of the instrumented optical modules. Since the final deployment of DOMs in 2010, novel modules have been developed. One of those new modules is the multi-PMT Digital Optical Module (mDOM) as illustrated in fig. 2.7.

In contrast to the DOM (fig. 2.6), featuring a single 10" PMT, the mDOM consists of 24 individual 3" PMTs. The total photocathode area thus increases by a factor of 2.16, which in term raises the detection efficiency since only photons hitting the photocathode will generate signals. The mDOM additionally implements reflectors around each PMT, compensating for photon loss caused by the holding structure.
Analysing individual PMT signals in comparison to a single larger one also yields superior photon counting. The total number of deposited photoelectrons is easier to obtain from individual hits, instead of from multi-photoelectron signal waveforms from a large PMT.

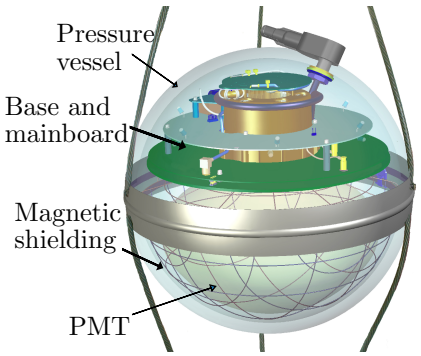

Fig. 2.6: Rendering of the DOM currently implemented in IceCube. Courtesy of the IceCube Collaboration.

The modules are protected by thick glass pressure vessels since the ice boreholes re-freeze from the top to the bottom due to the temperature gradient of the ice resulting in immense pressures. The glass vessels are rated to endure pressures of up to 700 bar. The associated thickness causes an obstacle because the transparency of the modules to low wavelength reduces. The intensity of the Cherenkov spectrum is proportional to λ^{-2}, reaching deep into the UV-region, meaning that a majority of the signal is absorbed by the glass enclosure. For a higher UV-transparency, improved borosilicate glasses are developed in order to increase the detected signals. Furthermore, the vessel glass contains trace amounts of radioactive isotopes such as ^{40}K as listed in table 2.1. These decays cause scintillation and Cherenkov light which causes an undesired background. This effect poses the motivation for this thesis in which the module background will be estimated for the given isotopes present in the glass.

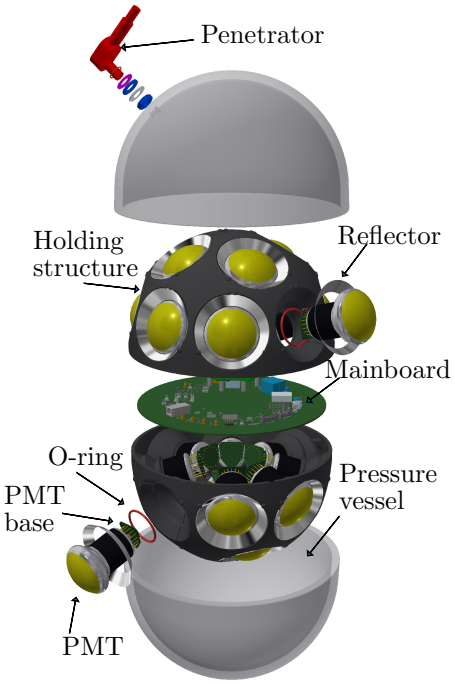

Fig. 2.7: Main components of the mDOM. Courtesy of the IceCube Collaboration.

Table 2.1: Activity per mass of three natural decay chains and ^{40}K of the 13 kg Vitrovex pressure vessel as measured in [10].

Decay	Activity (Bq/kg)
^{40}K	60.98 ± 0.86
^{238}U-Chain	4.61 ± 0.07
^{235}U-Chain	0.59 ± 0.05
^{232}Th-Chain	1.28 ± 0.05

2.2.2 IceCube Upgrade

The current stage of the detector development – *IceCube Upgrade* – is aimed to be fully completed in the Antarctic summer season of 2023. Within this scope, seven new strings will be densely embedded inside DeepCore as shown in fig. 2.8.

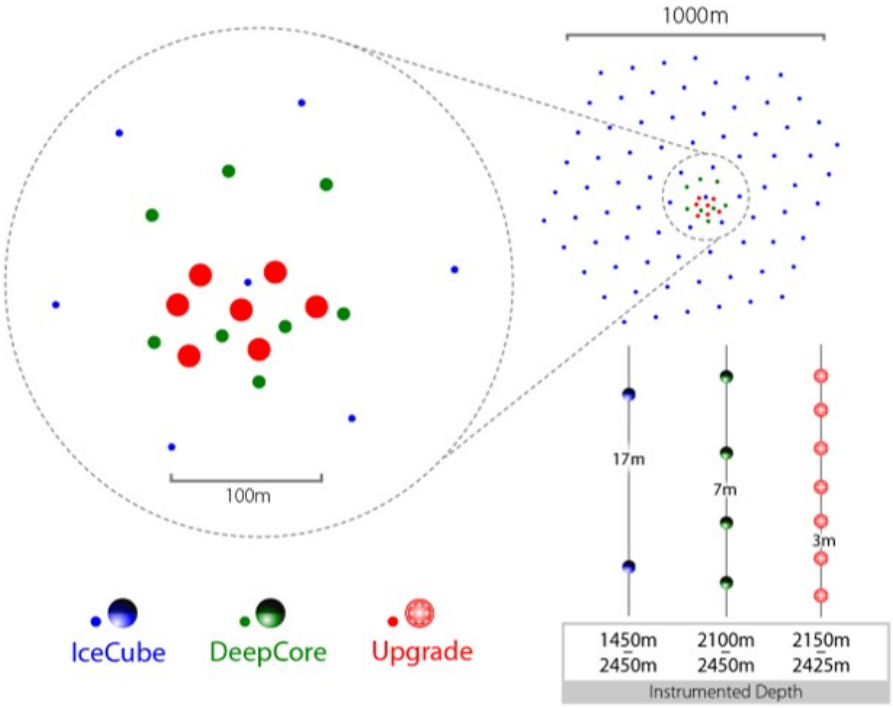

Fig. 2.8: Schematic of the proposed IceCube Upgrade. The blue dots mark the strings of the high energy array spanning the entire volume of instrumented ice. Inside of DeepCore (green), is the proposed pattern for strings of the Upgrade (red) in which the inter-module distance is even closer. Courtesy of the IceCube Collaboration.

The sensor density is higher, allowing for improved atmospheric neutrino event selection efficiency and reconstruction at energies of a few GeV. The aim of IceCube Upgrade is to provide world-leading sensitivity to neutrino oscillations and enable the detector to measure tau neutrino appearance with higher precision. Additionally, new devices such as cameras with flashers, and calibration LEDs are installed within the modules to improve the analysis of the optical properties of glacial ice and the module responses. The improved calibration will be applied to the entire archival data of IceCube from the last ten years [5].
Ultimately, over 700 advanced optical modules of different types (mDOM, D-Egg, and

pDOM to name the largest allocations) will be embedded into the ice to test their capabilities and potential improvements over current modules. These allow for improved detection efficiency and directional information on Cherenkov photons. In addition to the calibration devices integrated within the new modules, stand-alone devices such as the Precision Optical Calibration Module (POCAM) are planned to be utilised. This is an in-situ self-calibrating, isotropic, nanosecond pulsed light source primary planned to reduce systematic uncertainties (calibration of new/existing sensors and improved knowledge of glacial ice optical properties) [20].

3 Photomultiplier tubes

Photo**m**ultiplier **t**ubes (**PMT**s) are devices that convert single photons into a measurable electric signal which are crucial for IceCube's functionality and are the main tool for the sensitive measurements done in this work. In order to obtain reliable measurements, it is important to understand the operation principles and traits of this device.

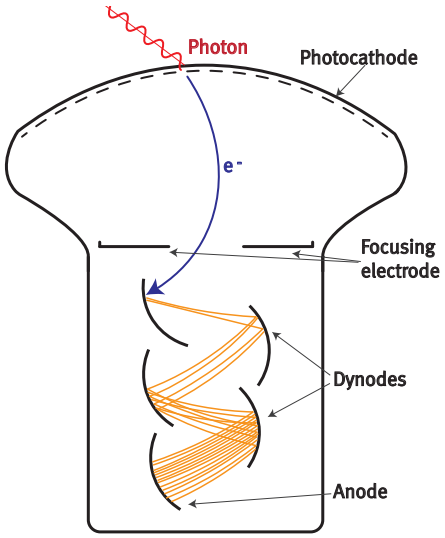

Fig. 3.1: Schematic of a PMT showing main constituents and the principle of photon detection. Figure taken from [10].

As a method to convert photons into predictable signals, a PMT utilises different stages as shown in fig. 3.1. An incoming photon absorbed in the photocathode - which is a thin layer of photosensitive material - can be converted into an electron inside of the vacuumed glass housing via the photoelectric effect. Through an external high voltage distributed by a base, the electrical components are interconnected with a potential leading electrons along the dynodes path to the anode.
The incident **photoelectron** is directed and electrostatically accelerated into the multiplier system by focusing electrodes whereafter it can strike the first dynode. Here, multiple **secondary electrons** are liberated from the dynode. Electrical fields gradually guide the various electrons onto adjacent dynodes and thus multiply the incident photoelectron exponentially. This step is necessary, because single electrons do not resemble signals strong enough to be measured. The last component in this system is the anode which will collect all arriving secondary electrons and output a signal proportional to their total number. There are two different operation modes for the read out of the resulting anode signal.
If information of individual pulses is not needed or if the PMT is continuously illuminated by an intense source of light, the PMT is operated in **current mode**. For a current output, the charge of pulses within a certain time window is integrated via a current-measuring device (e.g. picoammeter).
In photon-counting or **pulse mode**, single pulses can be analysed and thus enable the extraction of information on amplitude, charge, and time, thereby making it much more applicable for low-light measurements. In this mode, the anode signal is supplied to a resistor (e.g. inside an oscilloscope), which results in a voltage pulse.
Due to multitudes of different PMT types that vary in geometry and materials, it is crucial to define basic traits for the performance of this measurement device. These span over detection efficiency, time resolution, amplification, and various background signals. Furthermore, one can find slight variances in these characteristics between PMTs stemming from the same manufacturing batch which highlights the necessity to characterise PMTs for the following parameters.

3.1 Photocathode properties and quantum efficiency

Not every photon arriving at the photocathode will result in an emitted photoelectron within the PMT. This effect is quantified by the **quantum efficiency** and is defined as the ratio between all photoelectrons emitted from the photocathode to all incident photons striking it: $\mathrm{QE} = N_\gamma / N_e$.

Fig. 3.2 shows the effect of different entry windows and photocathode types on the quantum efficiency, whereas typical bialkali photocathode materials are Sb-Rb-Cs or Sb-K-Cs [21].
The glass entry window, on which the photocathode is evaporated onto from the inside, defines a lower wavelength limit to which the PMT can perform because of its inherent transmission spectrum. For borosilicate entry windows the cutoff lies around 300 nm whereas fused or synthetic silica like quartz may reach deep into the UV region. The choice of photocathode material primarily has an effect on the magnitude of the quantum efficiency i.e. lowering or rising it, in which the total photoelectron emission probability is wavelength dependant. While keeping the same spectral bandwidth, bialkali, super bialkali, and ultra bialkali show maximum quantum efficiencies of $\sim$ 25%, 35%, 43% respectively around 400 nm by improving the crystallinity [23]. Another possibility would be to choose multialkali photocathodes to gain a wider spectral range, but contrarily downgrading the quantum efficiency.

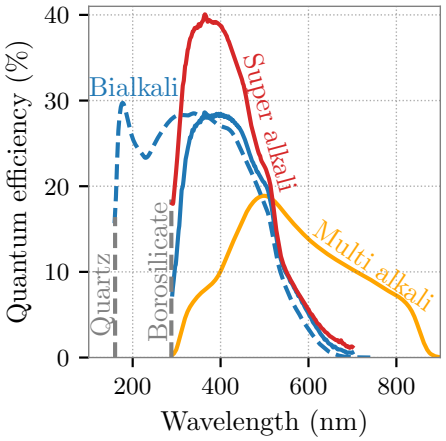

Fig. 3.2: Quantum efficiencies for different entry window materials (gray) and photocathode (coloured) types. There are far more variations than the exemplarily shown ones spanning optical ranges from 115 nm (Cs-I/Cs-Te) to 1700 nm (InGaAs) [21, 22].

3.2 Gain and collection efficiency

Photoelectrons travel through the multiplier system which comprises an array of metal electrodes – dynodes (made from e.g. AgMg, CuBe or NiAl [24]) – coated with a material featuring a high secondary emission coefficient, usually doped semiconductors with negative apparent electron affinity. Whenever accelerated electrons strike dynodes, secondary electron emissions occur, thus multiplying their total number. For each dynode one defines a secondary emission factor

$$\delta = \frac{N_{\mathrm{out}}}{N_{\mathrm{in}}} = a E_{\mathrm{p}}^{k}, \tag{3.1}$$

which gives the ratio of incoming electrons to the number of outgoing ones after secondary emission. This can be described by primary electron energy E_{p} which is proportional to the inter-dynode voltage, a PMT specific constant a, and an exponent $k \in (0.7, 0.8)$ indicating material and surface properties [21].

The **gain** g is the average total measurable number of secondary electrons, resulting from multiplications by the dynodes, reaching the anode after emission of one incident photoelectron. Totalling all dynodes, it results in the following relation:

$$g_{\text{ideal}} = \prod_{i=1}^{N} \delta_i. \tag{3.2}$$

It is titled as an *ideal* gain, since electron loss between dynodes is not included here. For this, a global **collection efficiency** is defined as $\text{CE} = g/g_{\text{ideal}}$ – the fraction of all produced secondary electrons to the measurable ones. This results in a Poissonian charge distribution respective to the number of photoelectrons which will be discussed in section 3.5.

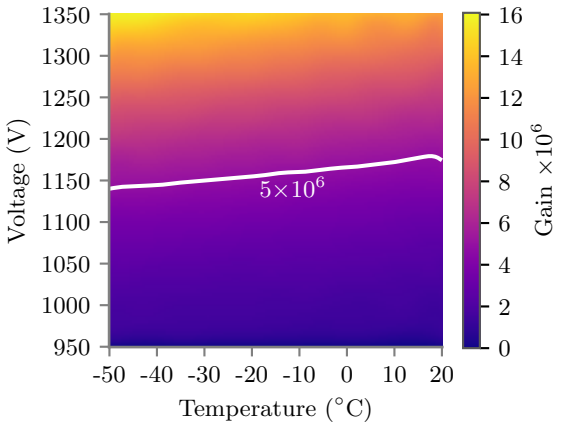

Fig. 3.3: Gain as a function of temperature and voltage (interpolated) from an exemplary measurement of a 3" PMT. The white line indicates the nominal voltage to achieve a gain of $5 \cdot 10^6$. Figure taken from [25].

Apart from the voltage dependence stemming from eq. 3.1, the gain is also a function of temperature, increasing to lower temperatures, as shown in fig. 3.3. This increase is believed to stem from an increase of the secondary emission coefficient of the dynodes [25].

In general, high value gains are favourable for higher signal-to-noise ratios (SNR) and to better distinguish between the number of incident photoelectrons. The **nominal** gain[1] is defined as $5 \cdot 10^6$ which is achieved by applying the *nominal voltage*, depending on the temperature.

3.3 Pulse timing parameters and pulse types

In pulse mode the anode signal results in a negative voltage pulse where the height is proportional to the number of secondary electrons at the anode and thus rises for higher light intensities, as well as for higher gains.
The mean elapsed time from the emission of a photoelectron to the deposition in the anode is referred to as the **transit time** and is mostly reliant on the overall size and supply voltage of the PMT. This arrival time is not a fixed value, as the geometry of the PMT, photon energy, and location of the illuminated part of the photocathode contribute to slight variations [24]. These deviations are specified by the **Transit Time Spread** (TTS) and define the time-resolution of the PMT. The arrival time distribution of the main peak can be approximated by a Gaussian distribution and consequently the TTS is defined by σ or the Full Width at Half Maximum: $\text{FWHM} = 2\sqrt{2\ln 2}\sigma$.

[1] Gains lie in order of $10^6 - 10^7$ for typical 3" PMTs, whereas the measurement and the PMT itself determines which value is suitable.

A **main pulse** is defined as an ordinary signal stemming from photoelectrons following the expected path (fig. 3.1). However, a main pulse can be replaced by early or delayed pulses and additionally be accompanied by early and late afterpulsing. These alternative pulse types are called **correlated background** and a histogram of arrival times is shown in fig. 3.4.

Early pulses or prepulses occur, if a photon permeates the photocathode and emits a photoelectron by striking the first dynode. Since the photoelectron is emitted further ahead within the PMT, this pulse will appear faster than main pulses, but is of smaller amplitude due to missing amplification of the first dynode.
A photoelectron can undergo backscattering at the first dynode without emitting secondary electrons. Due to the accelerating dynodes, it will be returned to the dynode for secondary emission with a time delay and lesser energy. Hence, **late pulses** are shifted by a few ns in respect to main pulses.
Early afterpulsing follows a leading pulse (including early and late pulses) if secondary electrons cause the emission of photons from dynodes by depositing energy. If this photon strikes the photocathode, it may cause an additional leading pulse with a time delay proportional to the distance of the luminescent structure to the photocathode.
At last, residual gas atoms (Ar, CO_2, He, ...) within the PMT can be ionised by electrons. Their positive charge accelerates them towards the photocathode where they may liberate several electrons, resulting in large pulses. Due to the high ion mass compared to electrons, this time offset of **late afterpulsing** arises in the scale of µs [27].

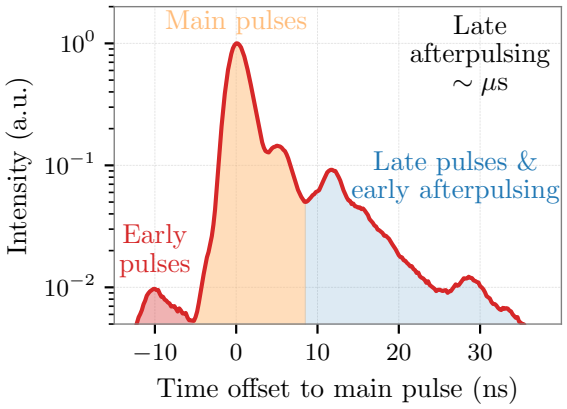

Fig. 3.4: Time histogram of PMT pulses in the vicinity of main pulses. The histogram shows leading pulses (early, main and late), whereas late pulses overlap with early afterpulsing. The secondary peak of the main pulses arise from the measurement since the entire hemispherical photocathode is illuminated. Taken from [26] and modified.

3.4 Uncorrelated background

Even if operated in complete darkness, a PMT will still produce measurable signals which perturb an actual measurement. This *random* background as illustrated in fig. 3.5 in combination with the correlated pulses from section 3.3 is called **dark rate** or **dark current** in pulse or current mode, respectively. The cause of the uncorrelated background will be explained in the following.

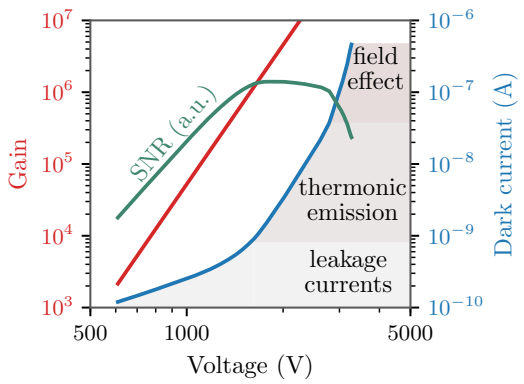

Fig. 3.5: Gain and anode dark current as functions of the PMT supply voltage, showing the voltage regions in which each of the three main causes of dark current predominates. The slope of the dark current overtakes the gain from certain voltages, resulting in an optimal-usage plateau of the SNR. The voltage domains for each effect will vary for different PMTs. Based on [24 (p. 15)].

At low amplifications and temperatures, **leakage currents** between electrodes on the glass and insulation surfaces dominate the dark current. External pollution like dirt, finger prints and humidity further contribute to this. These unintended current flows mostly occur between the anode and other electrodes as well as anode pin and other pins.
At typical gains ($10^5 - 10^7$), **thermionic emission** of electrons – mostly from the photocathode – is the main component of random dark noise. Thermionic emission varies with temperature according to the Richardson law $\propto T^2 \exp(-W/T)$, where W is the work function and can be drastically lowered by reducing the temperature T.
At excessive voltages, **field emission** (dynodes emitting electrons by the electric fields) will outweigh the previous effects. Besides, this may cause damage to the PMT, which is part of the reason why the maximum operation voltage is declared prior to this point. Additionally, the Signal-to-Noise-Ratio (SNR) will drop rapidly, thus making operation within this range not feasible by any means.
Lastly, electrons, radioactive isotopes like ^{40}K, and cosmic gamma rays striking the outer glass envelope may cause **scintillation** photons (see section 4.3) resulting in additional background. This property is temperature dependant in which the dark current rises towards lower temperatures [21, 22].

3.5 Single photoelectron spectrum

This section will explain how the charge distribution of a PMT is calibrated. Since it is possible that multiple photons strike the photocathode simultaneously and thus cannot be distinguished, it is necessary to be able to differentiate between pulses.
This type of measurement is performed in pulse mode with a pulsed light source. The PMT signal is externally triggered and integrated over a constant time window which results in a charge value proportional to the absorbed light.[2]
The construction and composition of a PMT charge distribution is illustrated in fig. 3.6. If the PMT does not detect a photon (0 phe), the charge value will solely consist of electronic noise and background effects as discussed in section 3.4. This baseline integration is referenced as **pedestal**. Whenever the PMT detects photons, the pulse will have a negative voltage value proportional to the number of emitted photoelectrons; this signal results in a greater charge. Since the gain is not a constant, mainly because of electron loss along the dynode path and secondary emission following Poisson statistics, the charge

[2] To obtain a charge in pulse mode, the integration value in units of Weber has to be divided by the input resistance of the oscilloscope.

q of $n > 0$ photoelectrons can be approximated with a Gaussian. In order to calibrate the charge spectrum, a PMT response function, developed by [28], is used.

In this method, the PMT response function $S_{\text{real}}(q)$ poses a convolution between an idealised PMT charge distribution expressed by Gaussians G and a background function B and is approximated by

$$S_{\text{real}}(q) \approx \exp(-\mu) B(q - Q_0) + \sum_{n=1}^{N} P(n, \mu) \cdot G(q - Q_0, Q_n, \sigma_n), \tag{3.3}$$

where Q_0 denotes the mean charge contribution of the pedestal. The background function is modulated by the probability of measuring no photoelectrons $P(0, \mu) = \exp(-\mu)$, being a Poissonian process due to photon emission from the light source, and models the pedestal for discrete background processes. The response for $n \geq 1$ photoelectrons is given by a Gaussian with a mean of $Q_n = nQ_1$ with spread $\sigma_n = \sqrt{\sigma_0^2 + n\sigma_1^2} \approx \sqrt{n}\sigma_1$, shifted by Q_0 and multiplied with the respective photoelectron probability $P(n, \mu)$.
In the aforementioned measurements, this PMT response function is fitted to the acquired charge distribution. From the obtained parameters, one is able to extract the mean number of photoelectrons μ, the spread of the respective phe distributions σ_n and, most importantly, the gain of the multiplier system. Once calibrated, as exemplarily shown in fig. 3.7, the gain can be derived by using the following relation:

$$g = \frac{Q_1 - Q_0}{e}, \tag{3.4}$$

e denoting the elementary charge.

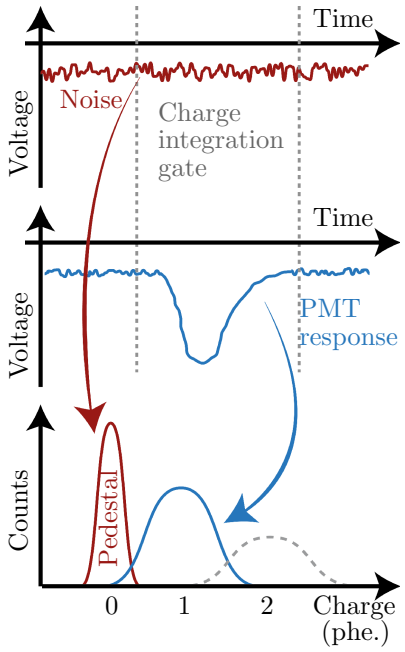

Fig. 3.6: Illustration of the charge spectrum acquisition. Figure taken from [10].

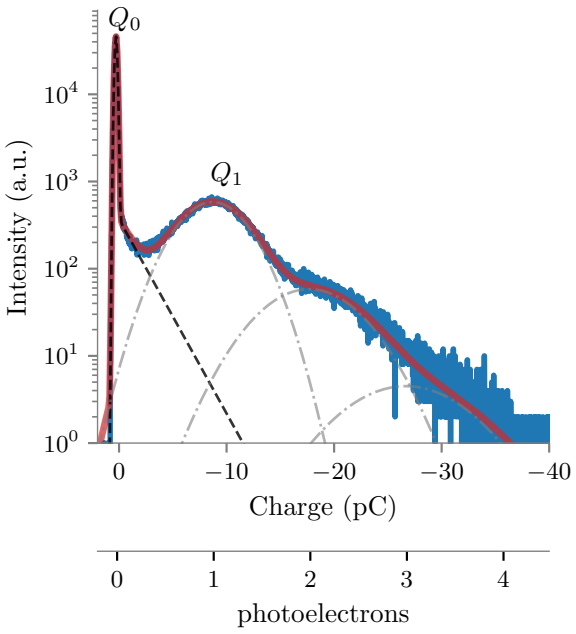

Fig. 3.7: Exemplary photoelectron-spectrum-fit (red) for a measured PMT charge (blue) where the n-phe peaks are shown in gray.

4 Interaction with matter

Since the isotopes within the pressure vessel produce α-particles, γ-particles and electrons, which cause scintillation (section 4.3) and Cherenkov (section 2.1.2) light, the fundamentals of interaction with matter will be explained in this chapter. In the later measurements, radioactive sources are used to induce more photon emissions from the vessel glass.

4.1 Gamma particles

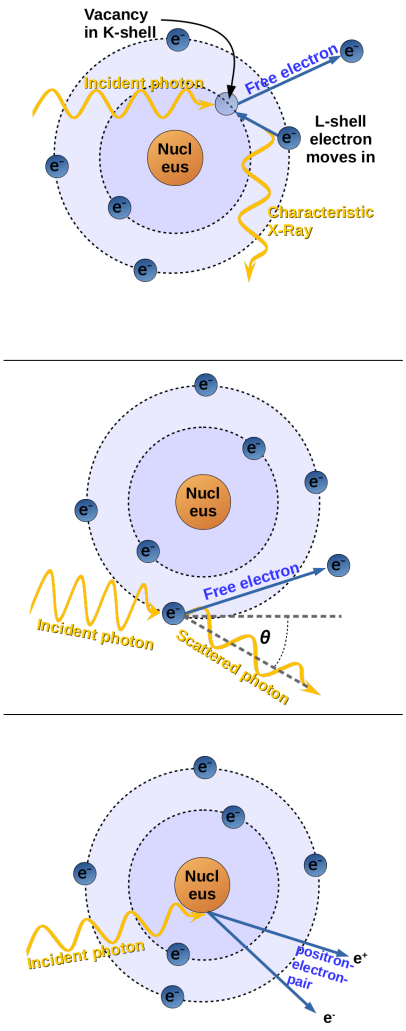

Fig. 4.1: Schematic of photoelectric absorption (PA) (**top**), Compton scattering (CS) **(middle)**, and pair production (PP) in nuclear fields (**bottom**).

Gamma interactions can be described as *all or nothing* events, since the γ will either pass through the target material or interact and therefore dissipate most of or its entire energy. The interactions are classified into three different subcategories as illustrated in fig. 4.1 dependant on the energy of the incident gamma.

The **photoelectric effect** dominates at low energies and describes the emission of an electron. If the photon energy exceeds the work function W of the material, an inner atomic shell electron is dislodged. This creates an ionised absorber atom with a vacancy in one of its bound shells. The leftover photon energy contributes to the free electrons kinetic energy $E_e = h\nu - W$. The cross-section σ is proportional to $Z^4 E^{-3.5}$ for low energies, Z denoting the atomic number [29].

Compton scattering is an example of inelastic scattering of photons with atomic electrons where the wavelength λ of the scattered photon undergoes the Compton shift:

$$\lambda' - \lambda = \frac{h}{m_e c}(1 - \cos\theta).$$

The energy transferred to the recoil electron $E_{e'}$ can vary from zero for $\theta = 0°$ to the maximum Compton electron energy

$$E_{e'} = E_\gamma \left(1 - \frac{1}{1 + \frac{2E_\gamma}{mc^2}}\right) + E_e \qquad (4.1)$$

for a photon angle of $\theta = 180\,°$ (backscattering). Compton scattering prevails in intermediate energies with a cross section $\sigma \propto \frac{\ln E}{E} Z$ [30, 31].

Pair production describes the conversion of a gamma into an electron-positron pair (positronium) by Coulomb fields either of nucleons or of atomic electrons. Hence, the required energy for pair production is larger than $2m_ec^2 + E_{\text{loss}} > 1.02\,\text{MeV}$ whilst excess energy is converted into kinetic energy. In the first case, only small energy fraction is lost to recoil energy of the nucleus, whereas a recoiling atomic electron can receive a sufficient amount of energy to emerge as an additional free electron (triplet production). The electron-position-pair is rapidly slowed down by the material until annihilation into photons occurs.[1] This process dominates high gamma energies and the cross section is $\propto Z^2 \ln(E)$ [31, 32].

The total cross section is expressed in form of a mass attenuation coefficient $\frac{\mu}{\rho}$ (area per mass) to describe how effective electromagnetic radiation is damped when traversing a material. The Beer-Lambert law is thus expressed via $I = I_0 \exp\left(-\frac{\mu}{\rho}\rho d\right)$, d denoting the penetration depth, ρ the density of the target material and I the intensity. The total photon attenuation is show in fig. 4.2 for borosilicate glass[2]. The reciprocal of the attenuation coefficient μ is the mean free path before γ-particles interact on average which equates to $\sim 5.9\,\text{cm}$ for $E_\gamma = 611.7\,\text{keV}$ in borosilicate glass.
The most important aspect of this section is that γ-radiation will produce electrons of lower energy within the target material.

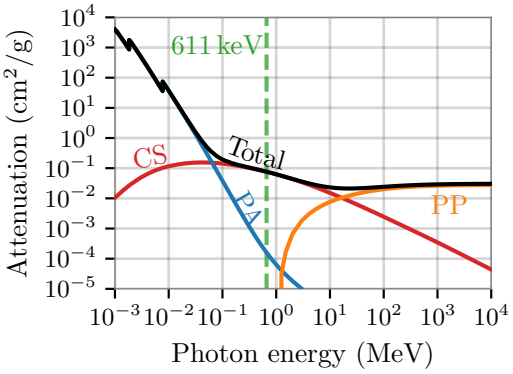

Fig. 4.2: Total Attenuation for photons in borosilicate glass subdivided into Compton scattering (red), photoelectric absorption (blue), and pair production (orange). Data acquired from [33].

4.2 Charged particles

The interactions of charged particles traversing an interaction medium dissects itself into excitation (elastic scattering from nuclei), ionisation (inelastic collisions with atomic electrons), bremsstrahlung (Gamma emission when the velocity or direction of electrons or protons changes), and Cherenkov radiation (see section 2.1.2). The energy loss per pathway within a medium is described by the Bethe-Bloch formula which is separated into light and heavy particles.
Heavy particle interactions are dominated by Coulomb interactions between the particle and the target atom which split into two electromagnetic processes: excitation and ionisation. The former is less common, since heavy particles deflect very little off electrons. Nuclear reactions are very unlikely and can be neglected altogether.
In case of ionisation processes, the kinetic energy of charged hadrons decreases after each interaction and will interact more strongly with atomic electrons as its energy depletes. For this reason, the deposited energy in the material increases with the travelled distance

[1] The time scale and number of emissions is dependent on the spin orientations, where one distinguishes between para- and ortho-positronium.

[2] The calculations in this chapter are done for Pyrex glass which includes the following compounds 80.6% SiO_2, 12.6% B_2O_3, 4.2% Na_2O, 2.2% Al_2O_3, 0.1% CaO, 0.1% Cl, 0.05% MgO, and 0.04% Fe_2O_3. This is a similar type of borosilicate glass as the latter investigated samples and has a mean excitation energy of 135.5 eV [34].

until the particles entire energy is dissipated (concluding with the Bragg peak). Single collisions mostly cause very low energy losses, but enough interactions occur to regard the cumulative energy loss. The mean rate of energy loss dE per pathway dx of the incident particle is referred to as **Stopping Power** and determined by the Bethe-Bloch equation as developed in [35]:

$$-\left\langle \frac{\mathrm{d}E}{\mathrm{d}x} \right\rangle = Kz^2 \frac{Z}{A} \frac{1}{\beta^2} \left[\frac{1}{2} \ln \frac{2m_e c^2 \beta^2 \gamma^2 T_{\max}}{I^2} - \beta^2 - \frac{C}{Z} - \frac{\delta(\beta\gamma)}{2} \right]. \tag{4.2}$$

$K = 4\pi N_\mathrm{A} r_\mathrm{e}^2 m_\mathrm{e} c^2 = 0.307\,\mathrm{MeVg^{-1}cm^2}$ is a constant, incorporating the electron density of the material and fine-structure constant α amongst other things, z is the charge of incident particle, Z of the target material, A its mass number and I the mean excitation potential. Equation 4.2 describes the mean energy loss, whereas statistical fluctuations would be described by the Landau distribution which consists of a Gaussian part and exponential tail towards large energy losses onto a single electron $T_{\max} = \frac{2m_\mathrm{e}c^2\beta^2\gamma^2}{1+2\gamma m_\mathrm{e}/M+(m_\mathrm{e}/M)^2}$. If the energy transfer is large enough, an electron is liberated from its atomic shell and may have enough energy to cause ionisation as well (**δ electrons**).
To calculate a realistic stopping power, a handful of corrections have to be applied however, for which the reader is directed to the literature provided in [34]. First, shell corrections C/Z are important when the velocity of the particle is not large compared to the velocities of the atomic electrons. Shell corrections for most elements are based on semi-empirical formulas developed by [36] and described in [37]. For elements with atomic numbers $Z > 63$, and for $Z = 47$, revised shell corrections from [38] are used. Second are the Barkas [39, 40] and Bloch [36] corrections, which take departures from the first-order Born approximation into account. And lastly, a density-effect correction $\delta(\beta\gamma)$ regarding a polarisation effect is considered which is not noticeable for the low energy cases at hand. For alpha energies lower than 2 MeV, the measured stopping power obtained by Anderson and Ziegler [41, 42] is interpolated with respect to atomic number and then fitted by the Varelas-Biersack formula [43].

Contrarily, electrons are considered **light particles** which mainly interact at the atomic level via ionisation and bremsstrahlung production. For electrons in the energy range from a few tens of electron volts to few MeV, the stopping power is governed by collision loss with other (atomic) electrons. At energies larger than several hundreds of MeV (critical energy) the bremsstrahlung effect from scattering processes becomes dominant due to the small mass of electrons. The basic mechanism of ionisation processes is likewise described by the Bethe-Bloch formula, but two essential changes have to be implemented.
First of, electrons have very small masses which means that they are easily scattered and complete back scattering can be significant especially in high-Z materials. Thus the assumption that the particle travels in a straight path is not valid anymore. Further, the assumption that each interaction resulting in energy loss is a small fraction of the incident energy is invalid since much energy is transferred in electron electron interactions. The second change that has to be regarded is that same particle interaction occur, so indistinguishability must be taken into account. The Bethe-Bloch formula adjusted for

electrons [44, 45] is expressed by

$$-\left\langle \frac{\mathrm{d}E}{\mathrm{d}x} \right\rangle_{\text{el.}} = K\frac{Z}{A}\frac{1}{\beta^2}\left[\frac{1}{2}\ln\frac{m_e c^2\beta^2\gamma^2 T}{2I^2}\right] + \left\langle \frac{\mathrm{d}E}{\mathrm{d}x} \right\rangle_{\text{Brems.}}$$
$$\text{with } \left\langle \frac{\mathrm{d}E}{\mathrm{d}x} \right\rangle_{\text{Brems.}} = 4\alpha\rho N_A \frac{Z(Z+1)}{A} z^2 \left(\frac{1}{4\pi\epsilon_0}\cdot\frac{e^2}{mc^2}\right)^2 E\cdot\ln\left(183Z^{-1/3}\right). \tag{4.3}$$

Here, T is the kinetic energy of the electron and the last term regards loss due to bremsstrahlung. The loss due to ionisation is $\propto \ln(\beta^2\gamma^2)/\beta^2 \propto \ln(E)$ and the radiative loss $\propto E$.

Equations 4.2 and 4.3 are multiplied with the density ρ of the target material from which the graphs in figs. 4.3 and 4.4 can be derived.

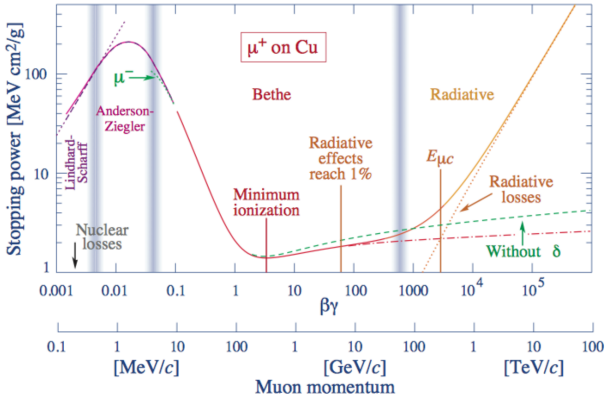

Fig. 4.3: Stopping power for antimuons within copper for energies from 100 keV to 100 TeV. The diagram shows all relevant processes depending on the energy regime. The Bethe-Bloch formula is valid within $0.1 < \beta\gamma < 100$. Figure taken from [46].

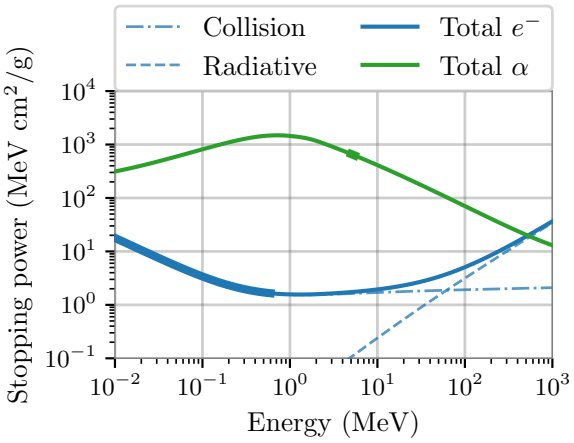

Fig. 4.4: Total stopping power for electrons and α particles in borosilicate glass subdivided into the different interaction processes. The broader sections of the lines correspond the energy of the alpha and gamma source used in the latter measurements. Data acquired from [34].

To summarise this section (regarding the energy of radioactive sources used later on), α particles will mostly lose energy due to ionisation and dissipate their entire energy in a few µm in the target. Furthermore, δ-electrons can be produced if sufficient energy is transferred. Electrons will also lose energy via ionisation within the samples and very rarely by bremsstrahlung if an electron with significant energy is generated. The continuous slowing down approximation (CSDA) range is $\sim 140\,\mu\text{m}$ for $E_e = 661\,\text{keV}$ and $\sim 27.5\,\mu\text{m}$ for $E_\alpha = 5.54\,\text{MeV}$ in borosilicate glass [34].

4.3 Luminescence

This section will explain the cause, working principle and dependencies of luminescence, with the main emphasis lying on scintillation of inorganic semiconductors by external excitation of high-energy particles. The principles explained in the following elucidate

the underlying physics of the main measurements performed within this work.
Luminescence is the umbrella term for light emission by materials not resulting from heat (cold-body radiation) which can be caused by a variety of different processes where one distinguishes between the type of excitation. The classification radioluminescence describes the excitation by ionising radiation such as alpha particles, high energetic electrons, or gamma rays. The resulting emission of photons with a characteristic spectrum by passage of such particles is dubbed **scintillation** which is an inherent material property and arises from the electronic band structure found in crystals.

4.3.1 Electronic transitions in semiconductors

Atoms in solid inorganic materials are arranged in a crystal lattice in which the discrete energy levels of atomic orbitals overlap. In macroscopic systems, each orbital splits into many different energy levels since the Pauli exclusion principle dictates that electrons cannot have the same quantum number in one state. Adjacent levels are condensed closely $\mathcal{O}(10^{-22}\text{eV})$ in which they are considered as a continuum. This energy band describes the range of energy levels that electrons may occupy within the solid. The highest occupied molecular orbital forms the valance band (VB) whereas the lowest unoccupied one represents the conduction band (CB). Energy states not populated in the atomic orbitals in the solid are termed band gap which separates the VB and CB with energy E_g [47].

When a particle deposits energy in this configuration an energetically favoured electron absorbs the energy $E_a > E_g$ and is promoted from its initial state E_i in the VB to an excited state E_f in the CB. While the electron moves in the lattice it leaves a tightly bound hole or recombination centre behind. The excited electron has a multitude of ways to dissipate the absorbed energy:
In **intrinsic** (band to band) transitions the energy is absorbed by the host lattice and the excited electron will spontaneously recombine back into its ground state by emitting a photon of energy $h\nu = E_i - E_f$. If the energy of the generated electron is below the ionisation threshold, the electron-hole-pair thermalises by intraband transitions via phonons, which are a quantified mode of local vibration surrounding atoms in the lattice [48].
In an ideal world, glasses are insulators with a large band gap, where solely intrinsic emissions occurs. But mechanical stress and change of temperature during the manufacturing process can cause the formation of defects such as dislocations and grain boundaries in the lattice where impurity atoms can also be embedded. The presence of defects changes the structural, electrical, and optical properties of materials which causes intermediate energy levels in the band gap [49]. These luminescent centres are called donor if energetically close to the CB with energy E_D which act as traps for electrons and acceptor with energy E_A if located near the VB, acting as a recombination site. The energy dissipation of electrons in this **extrinsic** case occurs step by step via these localised energy states or between multiple luminescent centres and opens the possibility for various transitions with different energies [50].

The absorption and subsequent emission of energy in **radiative** processes is illustrated in fig. 4.5 (left). The electron is excited with energy E_a in a broad optical band into a vibrational level m of excited state. Here, it relaxes to the lowest vibrational level via phonons (resulting in heat) where it will return to the ground state by emission of a photon

with energy E_e where vibrational levels n may be de-excited via phonons again, depending on the configurational coordinate of both states. These vibrational states stem from the Boltzmann distribution of charge carriers which results in an emission and absorption band instead of distinct spectral lines. The emission spectrum is further broadened by transitions between different orbitals of different ions. If no vibrational relaxations in the ground and excited state occurs ($n = m = 0$), the energy of the emitted photon is equal to the absorbed energy, which is commonly called zero phonon line. The energy $E_a - E_e$ otherwise depleted by phonons called Stokes-shift [49].

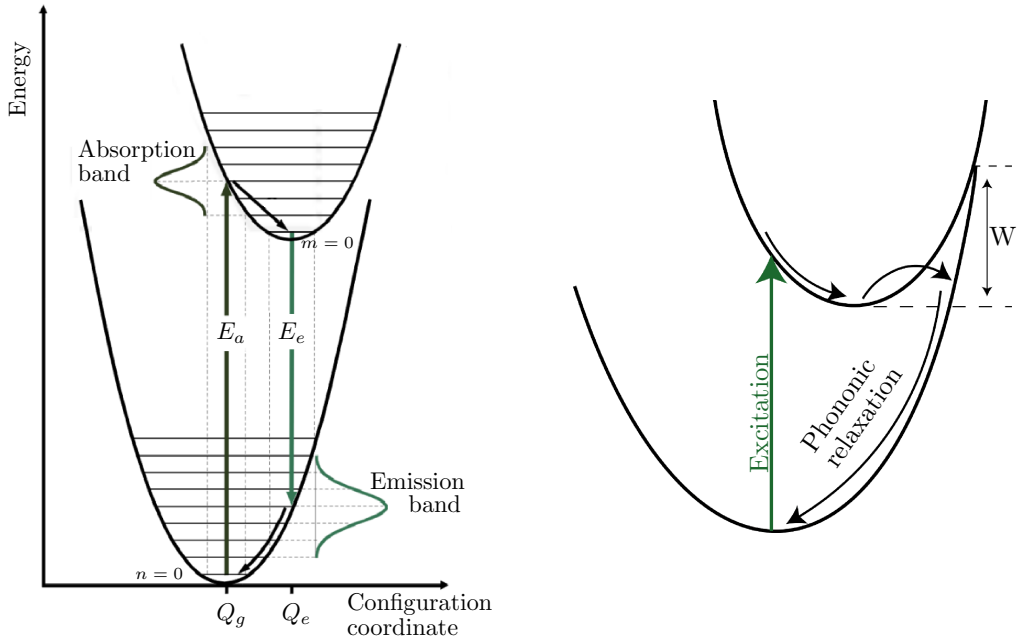

Fig. 4.5: Configuration coordinate diagram for photon emission (**left**) and a non-radiative recombination (**right**). The gap between Q_g and Q_e is the distance of nucleus between ground and excited state. Figures taken from [10].

Next to these (phonon assisted) photon transitions, there are a variety of **non-radiative** competing processes which are desirable regarding de-excitation in the vessel glass.
The dominant process is multi-phonon relaxation which describes the decay of excited electronic levels by lattice vibrations where (multiple) phonons are emitted to bridge the energy gap as shown in fig. 4.5 (right). If the ground state is thermally accessible by disposing the energy W, the electron can de-excite and relax vibrationally via phonons. The electron therefore thermalises which is coined **thermal quenching** with probability $P = C \exp\left(-\frac{W}{k_B T}\right)$ and decreases towards lower temperatures since less vibrational levels of ground state are populated [51, 52].

The timescale of these transitions is described by an exponential decay of rate τ, called the **lifetime**. The time distribution of decays resulting in photons in compounds is modelled with a multiexponential

$$I(t) = \sum_i \alpha_i \exp\left(-\frac{t}{\tau_i}\right). \tag{4.4}$$

The total intensity I is defined by the sum of all (radiative) transitions i present in the sample with respective intensity α_i [53].

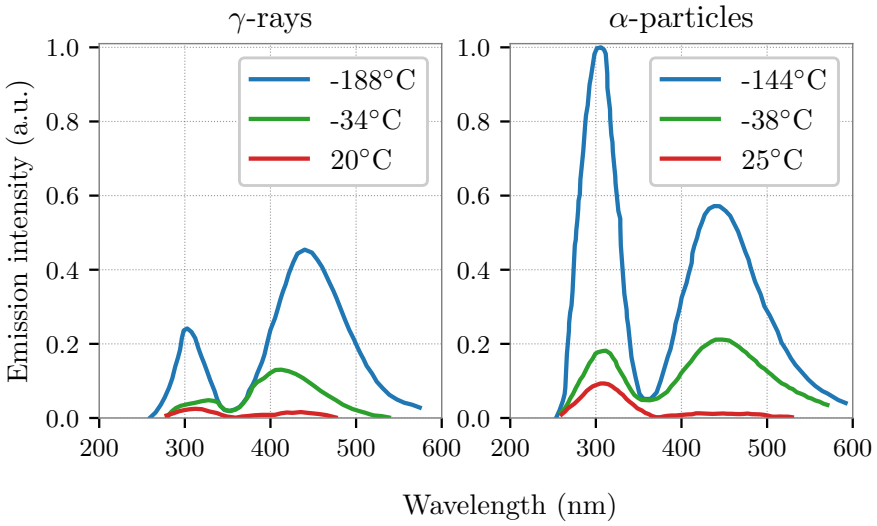

Fig. 4.6: NaI crystal doped with a concentration of 10^{-6} Tl, resulting in two separate emission bands. The activator suppresses the pure crystal emission band around 300 nm and causes an additional band at 430 nm. Data taken from [54 (p. 86)] and modified.

Scintillation is thus accompanied by a variety of different sub-processes and difficult to predict precisely. An exemplary emission spectrum is shown in fig. 4.6 for different temperatures, whereas the type of incident particle further varies the emission (discussed in section 4.3.2). The temperature dependant intensity of photon emission is mostly governed by the aforementioned thermal quenching. Since borosilicate glass consists of many compounds with unique properties, the total scintillation spectrum will be a broad overlap of every radiative recombination site.

4.3.2 Scintillation yield

It is inherently difficult to calculate a total recombination efficiency from every possible transition in complex compounds. Moreover, non-radiative processes such as multi-phonon de-excitation are not measured by PMTs and thus, the scintillation yield which gives a measure for all radiative recombinations is considered. The average expected number of luminescent photons

$$L = Y \cdot E \tag{4.5}$$

is described by the scintillation yield of the material Y (in units of MeV^{-1}) and deposited energy E. As the probability of radiative transitions raises towards lower temperatures because of thermal quenching, the scintillation yield scales accordingly.

This linear behaviour is however only valid for electrons with high energies, as the (specific) energy loss dE/dx for slower electrons and heavier particles such as alphas increases (see fig. 4.4). The differential form of eq 4.5 is

$$\frac{dL}{dx} = Y\frac{dE}{dx}. \tag{4.6}$$

Given a higher energy loss, the differential scintillation efficiency dL/dE is reduced below Y from above and thus the number of scintillation photons L increase non-linearly with E. This behaviour is attributed to quenching of the primary particle excitation by the high density $B\,dE/dx$ of ionised and excited atoms along the particle track is, where B is a constant. If quenching is considered uniform with a quenching parameter q, eq. 4.6 is modified to the semi-empirical relation

$$\frac{dL}{dx} = \frac{Y\,dE/dx}{1 + qB\,dE/dx}. \tag{4.7}$$

This is approximate to eq. 4.6 for particles with small energy loss dE/dx (fast electrons), and to

$$\frac{dL}{dx} = \frac{Y}{kB} = \text{const} \tag{4.8}$$

for higher losses. This relation thus predicts that for heavily ionising particles L varies with the residual range (and corresponding energy) of the particle in the scintillating material [54 (p. 185–188)].

Figure 4.7 shows a comparison of experimental data on the change of specific radiative scintillation against energy loss for electron, proton and alpha excitation in an organic scintillator. This shows that the amount of scintillation photons does not increase linearly for heavy charged particles and is attributed to luminescent centre saturation. Towards lower particle energies in a medium, there is an increase of specific ionisation density and local luminescent centres become increasingly saturated. The excess deposited energy is consequently lost to competing processes and with that, the scintillation yield progressively becomes almost independent of energy deposition given the asymptotic behaviour of eq 4.7. Overall, this causes light charged particles to produce more scintillation photons per deposited energy than heavy charged particles.

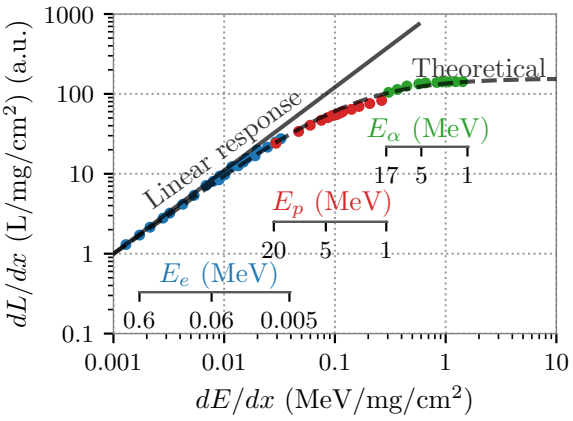

Fig. 4.7: Variation of specific luminescence dL/dx with energy loss dE/dx in anthracene crystals for electrons (blue), protons (red), and α-particles (green). The energy of the respective particle interacting with the medium is indicated by the scales. The theoretical curve corresponds to eq. 4.7 with saturated yield $Y = 1040\,\text{MeV}^{-1}$ and $qB = 6.6\,\text{mg}\,\text{cm}^{-2}\,\text{MeV}^{-1}$. Data taken from [54 (p. 188)]

Modelling the general scintillation response for inorganic crystal scintillators is an outstanding problem because eq. 4.7 is not applicable over the full range of $\frac{dE}{dx}$. The equation is further dependant on a factor $\frac{n_0}{n_e}$ which is the ratio of exitons resulting from recombinations n_0 to the total number of electron-hole-pairs n_e resulting from the deposited energy of the incident particle. This term is equal to one for organic scintillators but decreases for $\frac{dE}{dx} < 20\,\mathrm{keV\,mg\,cm^{-2}}$ in inorganic materials thus slightly decreasing the scintillation yield for electrons of varying energies. Due to the multitude of different influences in impurity activated scintillators, this effect has not been modelled accurately however and an extension of the ionisation quenching model to inorganic crystal scintillators is required whereas the organic description provides an appropriate approximation. Furthermore, the effects of luminescent centre concentration, temperature and δ-electrons have to be incorporated into a general theory. For more insight on this, the reader is referred to [54 (p. 431–470)].

To summarise, the scintillation yield is dependent on the temperature of the material and the particle type with respective energy. Moreover, it is highly reliant on the material itself since the ionic bonding and atomic structure gives rise to the electronic band structure which is altered by lattice defects and impurities. The scintillation response of organic scintillators is described by eq. 4.7 whereas inorganic crystal scintillators are not yet described by a general theory although they exhibit a similar behaviour such that α-particles cause a lower scintillation yield than electrons.

5 Modelling scintillation

The aim of this work is to determine scintillation characteristics of the mDOM vessel glass (brand *Vitrovex*) which will be used for background simulations of the optical modules. These parameters can be branched into the scintillation **spectrum**, **lifetime**, and **yield**. Preceding, these parameters were already determined in [10] for alpha radiation and a factor to scale the electron yield was assumed. But since α-particles and electrons interact differently with the glass (section 4.2) and thus cause respective photon emissions (section 4.3), the parametrisation has to be handled separately.

The spectrum is the energy distribution of the scintillation photon emission and is important for subsequent calculations of the yield. This was measured in [10] for (β^-) electron excitation which also produces undesirable Cherenkov light. To avoid this, the emission spectrum will be measured with alpha excitation in chapter 6.
The lifetime, which determines the time distribution of photonic de-excitations, will not be measured in this work. However, an estimation of the impact of the lifetime to the calculated scintillation yield is made in section 7.4.
The scintillation yield (expected number of emitted photons per deposited energy) for the samples provided by Nautilus (shown in fig. 5.1) will be measured and simulated for electron and alpha excitation. Due to the discrete interaction mechanism of gammas (see section 4.1) that result in electrons depositing the energy, a thicker sample irradiated by a γ-source is used to determine the electron yield. If energy loss from γ interactions is accounted for, the electron yield can be calculated from simulations.

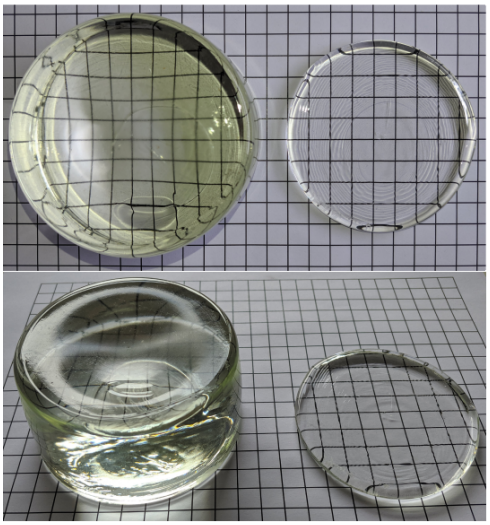

Fig. 5.1: Top and side view of Vitrovex borosilicate glass samples provided for this work. The thicker samples (five in total from two different manufacturing batches) are used for electron scintillation investigations and the thinner ones for alpha. The grid squares equate to $1\,\mathrm{cm}^2$.

For the alpha yield measurements, thinner and flatter samples are used to ensure optimal energy deposition into the sample. For correct simulations of the alpha yield, the electron yield has to be established first, since ionisation electrons are a by-product of alpha interactions.
In order to determine the scintillation yields, simulations are necessary since it cannot be derived from the measurements alone. This is accomplished by using *Geant4* which is a C++ based software toolkit, developed at CERN and KEK [55]. With this, particles passing through matter can be simulated whereas the various interaction processes can be chosen and modified if applicable. For the purposes at hand, the geometry, materials with respective properties such as absorption length and refractive indices, types of particles, interaction processes as well as the step size of the simulation for rapid processes like δ-electron emission from alpha absorption are specified.

In this thesis, a modified version of a simulation for the mDOM response, further adjusted in the framework of a master thesis for scintillation properties, will be used [10, 18]. The simulation takes the processes as listed in table 5.1 into account.

Table 5.1: Particles with corresponding physics processes accounted for in the simulation. The third column lists the respective Geant4 classes whereas the mDOMScintillation class is a modified version of G4Scintillation.

Particle	Process	Geant4 Class
Optical photon	Absorption	G4OpAbsorption
	Optical processes at medium interfaces	G4OpBoundaryProcess
	Mie scattering	G4OpMieHG
Gamma	Pair production	G4LivermoreGammaConversionModel
	Compton effect	G4LivermoreComptonModel
	Photoelectric effect	G4LivermorePhotoElectricModel
Electron	Scattering	G4eMultipleScattering
	Ionisation	G4LivermoreIonisationModel
	Brehmsstrahlung	G4eBremsstrahlung
	Cherenkov radiation	G4Cerenkov
	• For positron: annihilation	G4eplusAnnihilation
Ions	Scattering	G4hMultipleScattering
	Ionisation	G4ionIonisation
	Radioactive decay	G4RadioactiveDecay
Alpha	Scattering	G4hMultipleScattering
	Ionisation	G4ionIonisation
All particles above excepting photons	Material scintillation	mDOMScintillation

6 Scintillation spectrum

In this chapter the scintillation spectrum of the vessel glass induced by α-particles is measured. In order to simulate the behaviour of scintillation parameters correctly, the emission spectrum of the sample has to be implemented since the quantum efficiency of the PMT is wavelength dependant and the emission probability of specific wavelengths will thus influence the number of expected PMT hits in the later simulations.

6.1 Measurement setup

One can calculate the relativistic kinetic energy of a charged particle needed to induce Cherenkov radiation in a medium by applying the condition $\beta > n^{-1}$ to eq. 2.2 as follows:

$$E_{\text{kin}} = m_0c^2 \left(\frac{1}{\sqrt{1-\beta^2}} - 1 \right) > m_0c^2 \left(\frac{1}{\sqrt{1-\frac{1}{n^2}}} - 1 \right) = m_0c^2 \left(\sqrt{\frac{n^2}{n^2-1}} - 1 \right). \quad (6.1)$$

Accordingly, the energy threshold is solely determined by the refraction index of the medium and the rest energy m_0c^2 of the charged particle. Table 6.1 shows an overview of energy thresholds for electrons and alpha particles traversing ice and borosilicate glass:

Table 6.1: Kinetic energy threshold for electrons and alpha particles in different media ($n_{\text{ice}} = 1.33$ and borosilicate glass $n \in (1.48, 1.54)$) to induce Cherenkov radiation. The required energy is solely dependent on the rest energy m_0c^2 of the particle within a medium, as denoted in the last row.

	Cherenkov threshold (MeV)		
Particle	$n = 1.33$	$n = 1.48$	$n = 1.54$
e	0.28	0.18	0.16
α	2042.78	1328.77	1173.91
E/m_0c^2	54.8 %	35.6 %	31.45 %

To adequately excite the Vitrovex sample, an ^{241}Am source ($E_\alpha \approx 5.64\,\text{MeV}$) is used due to the high Cherenkov threshold for alpha radiation and thus an unadulterated scintillation spectrum can be obtained. For this purpose, it is not necessary to know the activity of the source as the intensity of radiation does not affect the photon emission distribution. However, the activity has to be considerably high in order to generate as many scintillation photons as possible for reliable measurements. Possible electrons produced by interactions of the gamma de-excitations of the excited decay product $^{237}\text{Np}^*$ ($E < 0.16\,\text{MeV}$) fall below the Cherenkov threshold.

In order to be sensitive to the entire emission spectrum, UV-transparent components have to be used in the measurement.

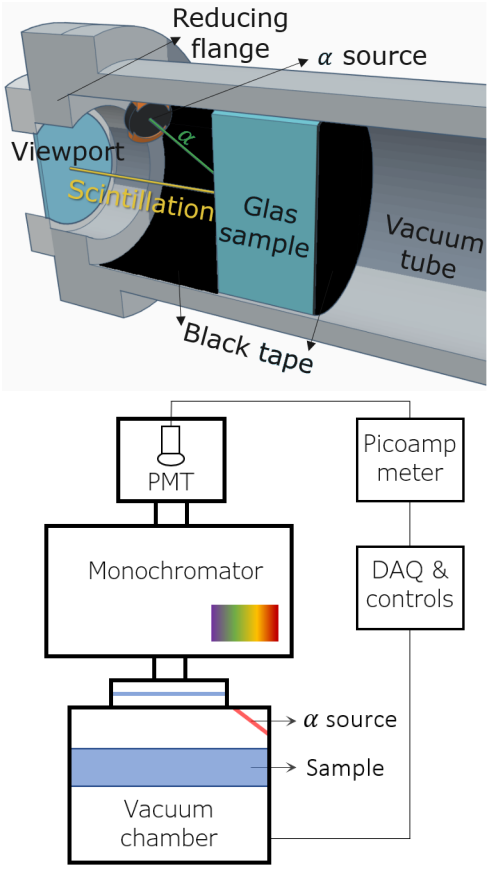

Fig. 6.1: (**Top**) Cross section view inside of the vacuum tube to illustrate how the sample is excited. (**Bottom**) Measurement setup to obtain the scintillation spectrum.

The setup is illustrated in fig. 6.1 showing the scintillation photon generation and the main components used for recording the spectrum.
Since α-particles cause air scintillation, this measurement is performed under vacuum[1]. In order to verify if the pressure is adequately low, has to be reviewed in a background measurement however.
The source is orientated to the sample where the deposited energy causes scintillation. To circumvent transmission of photons travelling through the glass, which would result in a wavelength shift, the sample is irradiated from the detector side since α-particles only penetrate the sample on orders of µm depth (section 4.2). Furthermore, the backside of the sample and the vacuum tube walls are covered with black non-reflective tape to prevent measuring reflected photons.
The scintillation light passes through a viewport[2] and is guided through a monochromator[3] to filter and measure wavelengths independently. The sample is placed as close to the source as possible while maintaining maximum central photon output through the viewport into the monochromator slits. On the opposite side, the light intensity is measured by a PMT[4] operated in pulse mode and read out by an oscilloscope[5] from which the signal rate is obtained.
The opening and exiting slits of the monochromator are adjustable (a few µm to 15 mm) to introduce more light, however, with the side effect of worsening the wavelength resolution as halving the opening of both slits results in quadrupling the resolution [10]. Since the amount of light reaching the PMT is fairly low, the monochromator slits have to be adjusted to an opening of 7.5 mm which results in a resolution of $\Delta\lambda = 17.5$ nm.

6.2 Spectrum measurement

The data is acquired by scanning wavelengths from 200 nm to 590 nm in increments of 15 nm. The PMT rate is measured multiple times for each wavelength while the dark rate is measured twice at 1200 nm where the PMT is not sensitive anymore. The entire process is repeated over 500 times for significant statistics since the amount of detected light is low as mentioned before. The dark rates from all consecutive runs are fitted with a linear function to be subtracted from the wavescans for a given run.

[1] The vacuum strength is $< 10^{-6}$ bar (Trivac D16A pump).
[2] VAB Sapphire VCF63.
[3] LOT-QuantumDesign MSH-300.
[4] Hamamatsu R8520-406 (SEL).
[5] Waverunner 8404M-MS

Previous trials have shown that the activities of available α sources are not high enough to yield substantial results. In order to maximise scintillation light, two ^{241}Am sources ($A \approx 360\,\mathrm{kBq}$ and $A \approx 400\,\mathrm{kBq}$) deposit approximately $\sim 1\,\mathrm{TeV/s}$ of α radiation into the sample. In contrast to fig. 6.1, the sample is brought as close to the viewport as possible to ensure maximum number of photons entering the monochromator.
The acquired data of complete scans for the measurement and the background is shown in fig. 6.2. The blue lines represent the entire data set from each run, whereas the red points indicate the mean PMT rate of each wavelength weighted by the respective frequency. The background measurement is taken by removing the sample whilst only potential photons from air scintillation are measured. The emission of photons following air scintillation would be detrimental to this measurement since both spectra lie within the same wavelengths [56]. Fortunately, no measurable background is present in this setup.

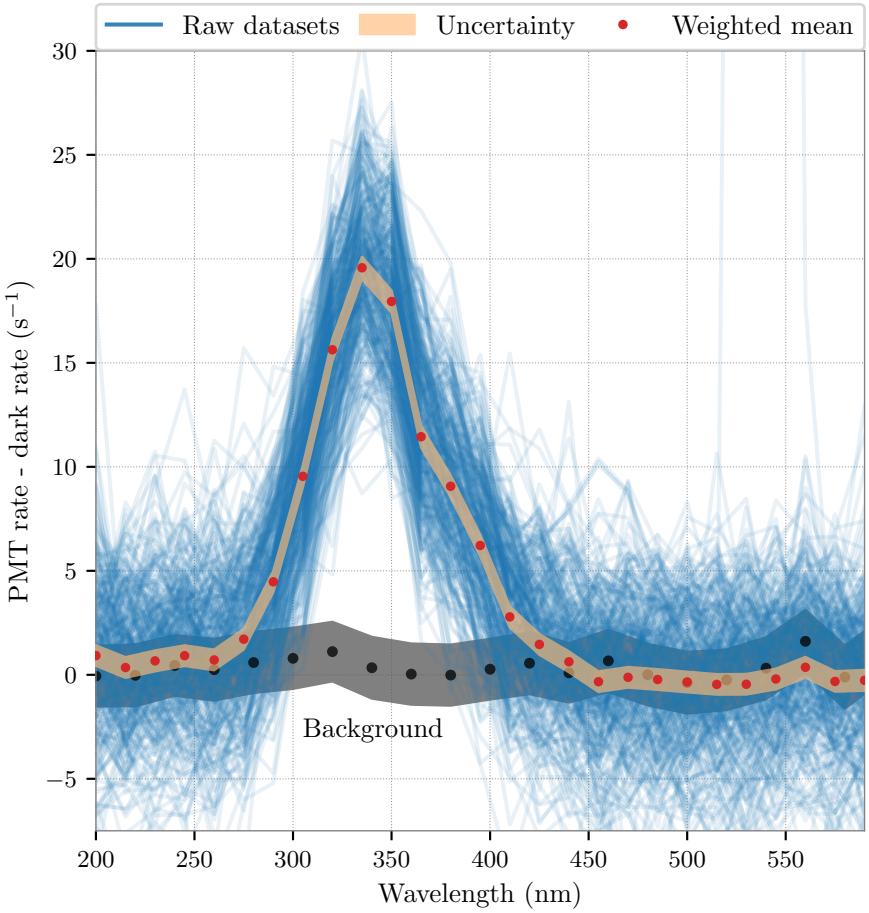

Fig. 6.2: Scintillation rates for each wavelength (blue), weighted mean (red) with the respective uncertainty (orange), compared to the background (black) which is measured with less runs.

The maximum of the spectrum lies at $(340.0 \pm 4.3)\,\mathrm{nm}$, corresponding to a photon energy of $(3.64 \pm 0.05)\,\mathrm{eV}$, and the emission of scintillation light occurs between 260 nm-450 nm. In an ideal world glass is an insulator with a large band gap and thus only intrinsic emission should occur. However lattice defects and impurities in the glass result

in additional (lower) energy levels causing supplementary extrinsic emissions. The measured spectrum is a broad superposition of various radiative transitions from which more scintillation photons are released compared to the exclusively intrinsic case.
This measurement is however impacted by all optical components where the respective properties have to be corrected for.

6.3 Corrections

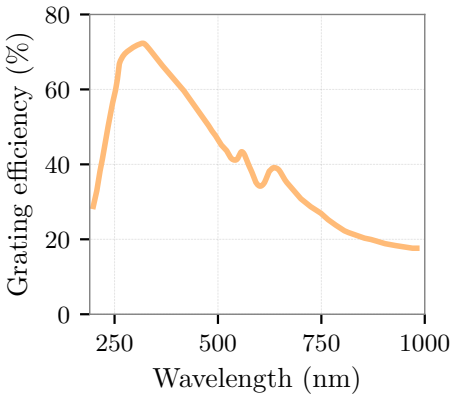

Fig. 6.3: Monochromator grating efficiency as provided by the manufacturer.

The first correction that has to be applied is the diffraction or grating efficiency $GE(\lambda)$ of the optical grating of the monochromator. It states the transmission of light for each wavelength and the manufacturer data is shown in fig. 6.3.
Next, the quantum efficiency of the PMT has to be determined. To accomplish this, the measurement as illustrated in fig. 6.4 is performed with a PMT base that interconnects the entire multiplier system so that each photoelectron striking the multiplier system is collected but not multiplied. This means that, due to the lack of amplification, the PMT is illuminated by an intense light source and it is driven in current mode, integrating the photoelectrons during a certain time window. The light source is a xenon lamp[6] emitting white light, a super-imposition of a vast range of wavelengths, which is guided through the monochromator. To determine the intensity of the light per wavelength, a reference photodiode[7] measures the light flux. This photodiode was calibrated by Newport and thus its QE is known. The monochromator is cycled through 200 nm to 750 nm in increments of 5 nm, whereas the slits are adjusted to 1 mm ($\Delta\lambda = 4$ nm) in this setup for higher precision. The diode is retracted out of the beam by a motor to illuminate the PMT which is measured in current mode subsequently. The dark currents of both devices are measured by a picoammeter[8] when they are outside of the beam or covered by the diode respectively. This cycle is repeated ten times and weighted.
The quantum efficiency $QE(\lambda)$ of the PMT is calculated by

$$QE_{\mathrm{PMT}} = \frac{I_{\mathrm{PMT}} - DC_{\mathrm{PMT}}}{I_{\mathrm{Diode}} - DC_{\mathrm{Diode}}} \cdot QE_{\mathrm{Diode}} \tag{6.2}$$

where I denotes the respective current for a given wavelength and DC the dark current. The resulting quantum efficiency is shown in fig. 6.5. The maximum lies at 335 nm (33.2 %) and the cutoff would start at a wavelength lower than 150 nm in comparison to conventional bialkali PMTs with a borosilicate window. Unfortunately, the cutoff cannot be measured with this setup since the xenon lamp does not produce significant output for wavelengths < 240 nm which has to be excluded from the data.

[6] LOT LSE140 / 160.25C.
[7] Newport 818-UV.
[8] KEITHLEY 6482.

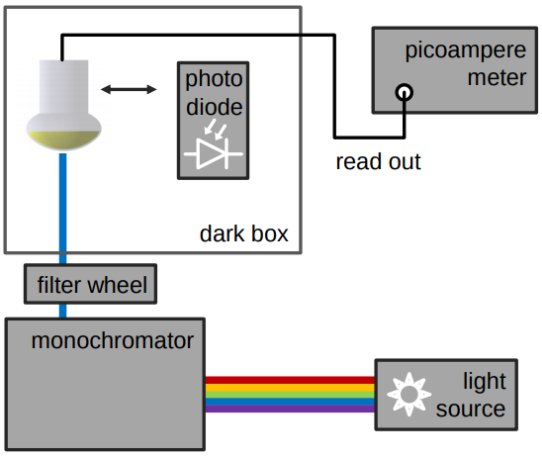

Fig. 6.4: Setup used for the quantum efficiency measurement. Figure taken from [18].

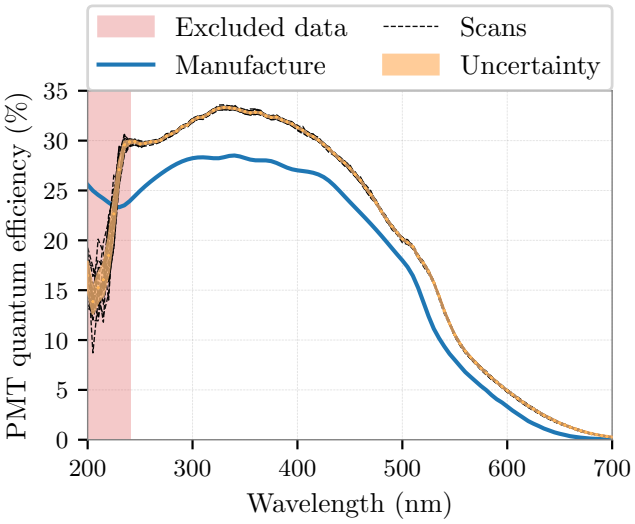

Fig. 6.5: Quantum efficiency of the UV sensitive PMT. The higher values compared to the average manufacture specification arises because this PMT is selected from batches to have a high QE, as denoted by the affix *SEL* on the PMT.

Lastly, the viewport has a wavelength dependent transmission $T(\lambda)$ that reduces the photon number exiting the vacuum tube. In order to measure this property, the QE setup (fig. 6.4) is used again whereas the photodiode is replaced by the viewport which is simply directed into and retracted out of the light beam. The PMT is measured twice and the respective signals are divided. The results are shown in fig. 6.6 in which the data below 240 nm has to be excluded once again because of the xenon lamp output.

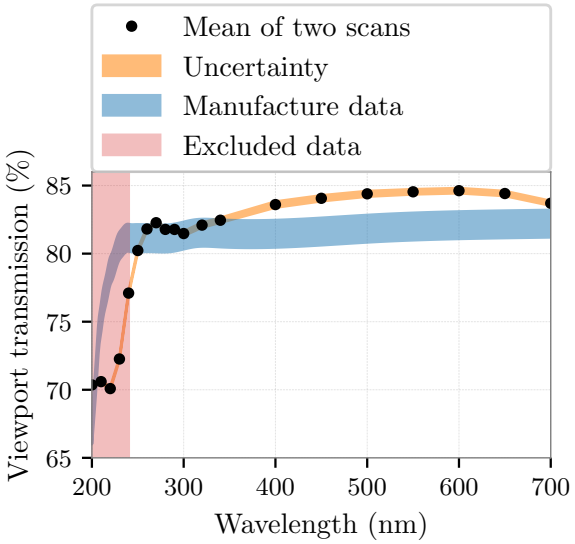

Fig. 6.6: Transmission of the viewport as measured and compared to the manufacturer data.

All corrections pose simple divisions applied to the measured spectrum $S_m(\lambda)$ by

$$S_c(\lambda) = \frac{S_m(\lambda)}{QE(\lambda) \cdot GE(\lambda) \cdot T(\lambda)}, \tag{6.3}$$

whilst the corrected spectrum $S_c(\lambda)$ is shown in fig. 6.7. The spectrum is normalised, since the emission probability for the wavelength of photons after excitation is of interest, in contrast to the PMT response of this specific setup.

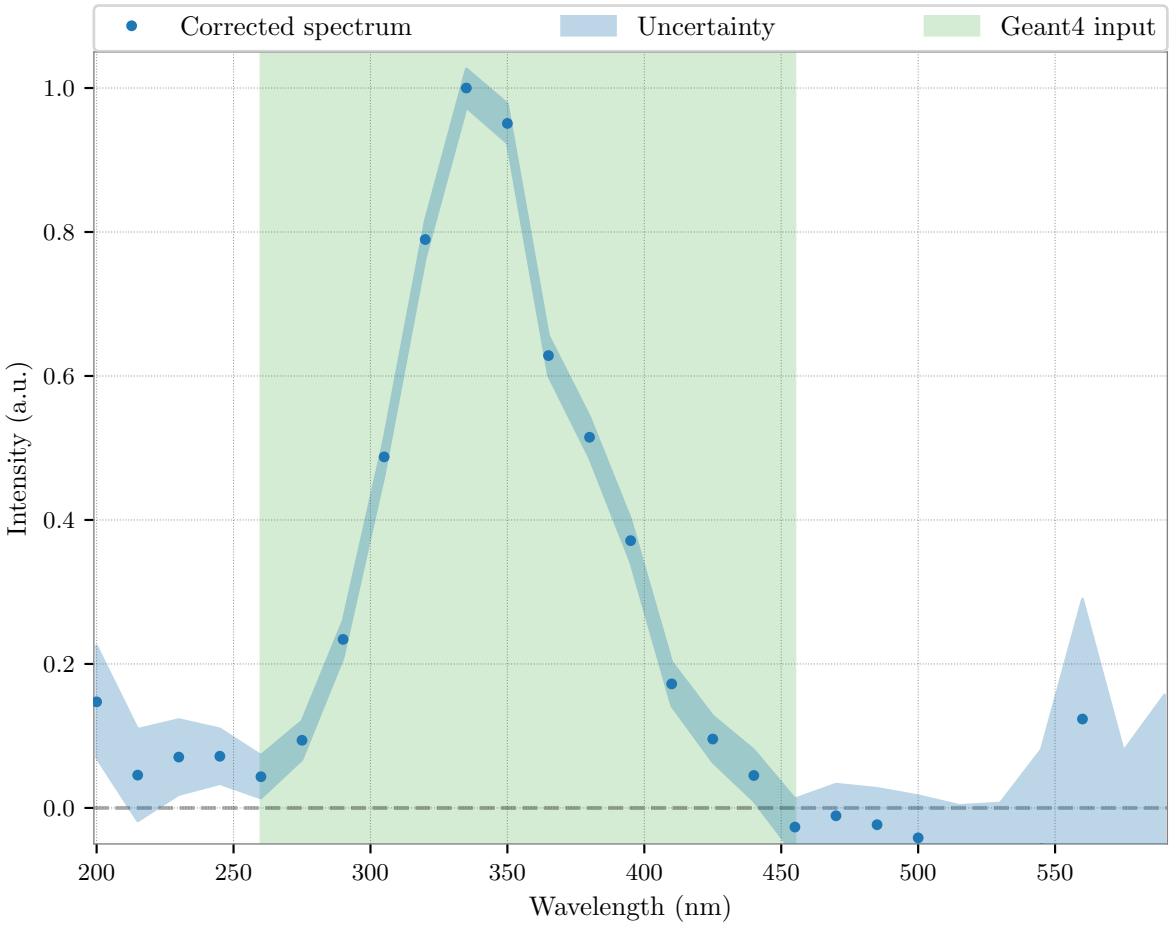

Fig. 6.7: Corrected scintillation spectrum $S_c(\lambda)$ of the Vitrovex glass sample.

The region of interest lies between 260 nm and 460 nm since no scintillation light is detected outside of this interval even though all components are still sensitive. The non-zero values may be explained by scattered light within the monochromator and susceptible PMT base noise. Furthermore, the dark rate fluctuated between the runs and could explain the perceptible slope. Lastly, the corrections below 260 nm are not factual since the xenon lamp does not emit enough light in this range which results in an amplification of noise.
The highlighted region will be a parameter for the yield simulations in the later studies.

For a wavelength resolution of $\Delta\lambda = 17.5\,\text{nm}$ the signal-to-noise ratio results in 1.16 at the maximum in this setup. For reliable measurements with higher resolutions to e.g. better resolve the lowest emission wavelength or distinct peaks, the SNR can be approximated by the following relation:

$$SNR = \underbrace{\eta \cdot E_\alpha \cdot Y_\alpha}_{\text{const}} \cdot A_\alpha \cdot (0.01 \cdot S^2) \cdot (1 - \exp(-0.4 \cdot t_{\text{meas}})).$$

A_α is the activity of the alpha source with an energy of E_α, Y_α the respective yield and η resembles the setup efficiency which is not trivial to determine. Not only does the fraction of α-particles depositing energy in the sample matter, but also the emission of scintillation photons in alignment with the monochromator slits. The term $(0.01 \cdot S^2)$

considers the wavelength resolution in terms of monochromator slit opening that reduces the light throughput. For a slit opening of 10 mm, the value is 1 and for each halving of the slits, the amount of light is reduced by factor 4. Thus slits with e.g. 1.25 mm opening have $\frac{1}{4^3}$ less light passing through the monochromator. The last term expresses the fact that the measurement is more precise for longer measuring times t_{meas} (given in weeks) which is estimated by the size of the uncertainty.
Assuming a precision of 80 % from the four week measurement shown in fig. 6.2, the constant is determined to roughly $3.4 \cdot 10^{-7}$. If an SNR of at least 2 (which should be the absolute minimal signal strength to aim for) at the maximum of the spectrum is to be obtained with a resolution of 5 nm ($S = 1.8$ mm), one needs to measure 8 weeks with a source activity of 189 MBq, if the setup efficiency cannot be improved further.

7 Scintillation yield for electrons

In order to determine the scintillation yield (see section 4.3.2), the glass samples are excited by radioactive sources resulting in intense emissions compared to the trace amounts in the glass as listed in table 2.1.

For the electron yield, the chosen source is ^{137}Cs which is mono-energetic (E_γ = 611.7 keV) and has stable decay product, ^{137}Ba. The source is enclosed and thus β^- decays are absorbed by the shielding material while γ-particles are emitted after the de-excitation of barium and produce electrons in the glass.

7.1 Quantifying scintillation emissions

7.1.1 Measurement

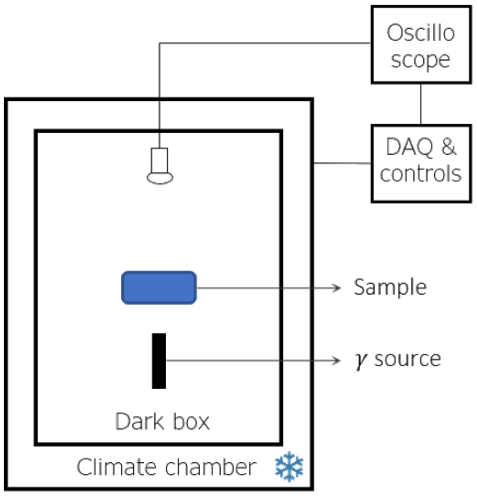

Fig. 7.1: Measurement setup for the electron scintillation yield by investigating PMT rates in a climate chamber.

To measure the amount of scintillation light, the setup as shown in fig. 7.1 is used.
Since the probability of de-excitation via photons rises towards lower temperatures in contrast to phonons (see section 4.3), the yield will show this temperature dependence as well. Thus the setup is located within a climate chamber[1] which is set to temperatures from -50 °C to 20 °C in increments of 10 °C.
The PMT[2] driven at nominal voltage, the glass sample, and the ^{137}Cs gamma source are centrally aligned and the respective spacing in between is measured. Once the temperature within the chamber maintains a constant level, the PMT rate is measured for 3 h.
The measurement is set up to continuously record sample intervals up to 1 ms from a randomly timed trigger and thus pulses are acquired in *real time*. For each pulse, the time, amplitude, and charge is recorded by which the number of pulses in the sample interval can be calculated from which the rate is derived. The dead time is set to 20 ns to avoid recording pulse ringing as additional signals. Before supplying the signal to the oscilloscope[3], it is amplified[4] by a factor of 4 to allow for a lower trigger threshold ($\sim$ 0.15 phe).[5] How the trigger is determined will be explained in section 7.3.

[1] CTS C-70/350.
[2] Hamamatsu R12199-01 HA MOD.
[3] PicoScope 6406C.
[4] CAEN Mod N979B.
[5] The amplification factor was verified by comparing the PMT gain from charge calibrations for different temperatures and supply voltages with and without the amplifier.

To measure the background of this measurement, the PMT is shielded by a thin light-proof cover, thus blocking all arriving (scintillation) photons while residual γ-particles that penetrate the sample still result in the same amount of signals within the PMT. The cause of these signals is not known but may stem from scintillation of the glass envelope, excitation of the photocathode, or release of photoelectrons from gammas interacting with the dynodes. This background rate does not only stem from gammas but the inherent PMT dark rate is also included.

An exemplary result is shown in fig. 7.2. Here, the respective rates are measured twice (cooling down and heating up) to verify whether the rates are identical for a given temperature. In the preceding measurements the temperature region of interest lies below -15 °C since the scintillation lifetime was measured only in this temperature range. Additionally, these results are aimed to be used for module simulations within IceCube's ice temperatures. For these temperatures, the PMT rate shows a linear behaviour as indicated by the lines and the rate increase due to scintillation photons is acquired by subtracting the background rate.
This measurement is performed multiple times for different samples and varying spacing between the three components to rule out systematic errors which will be presented in section 7.3.

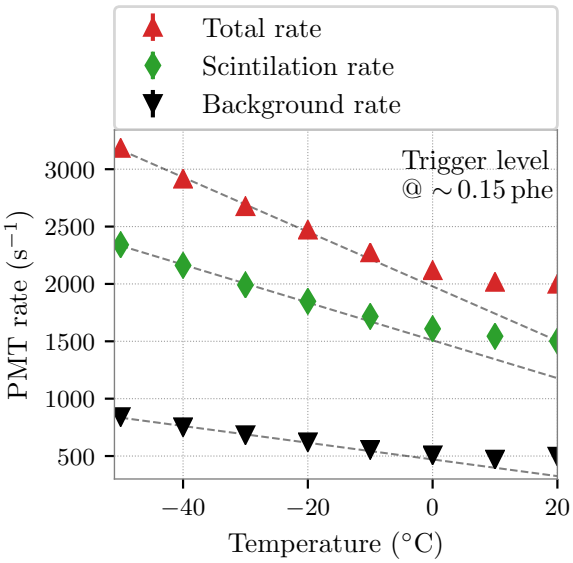

Fig. 7.2: Measured PMT rates from an exemplary setup for temperatures from -50°C to 20°C in increments of 10°C. The scintillation rate (green) is acquired by subtracting the background (black) from the total rate (red).

7.1.2 Afterpulsing-Correction

As discussed in section 7.1.1, solely PMT rates due to scintillation should be accounted for when calculating the scintillation yield. However, afterpulsing increases the measured rate which is not simulated. Hence, the calculated scintillation yield would show a higher value than in reality.
To better visualise this impact and the overall background of correlated PMT pulse influence, $\log_{10}(\Delta t)$ representations are advantageous. The PMT signals consist of correlated pulses (multiple scintillation photons caused by the same decay and afterpulsing) and uncorrelated ones (PMT dark rate and scintillation photons caused by different decays). The latter are a Poissonian process with an average rate μ since events are independent of previous signals. The time difference between subsequent photons shows an exponential decay in which the participating correlated background is distinguishable in a linear representation. When regarding the logarithm of time difference between subsequent hits $\log_{10}(\Delta t)$, however, a maximum lies at $x = -\log_{10}(\mu)$. An example of this representation is shown in fig. 7.3 where uncorrelated and correlated photons can be distinguished particularly well.

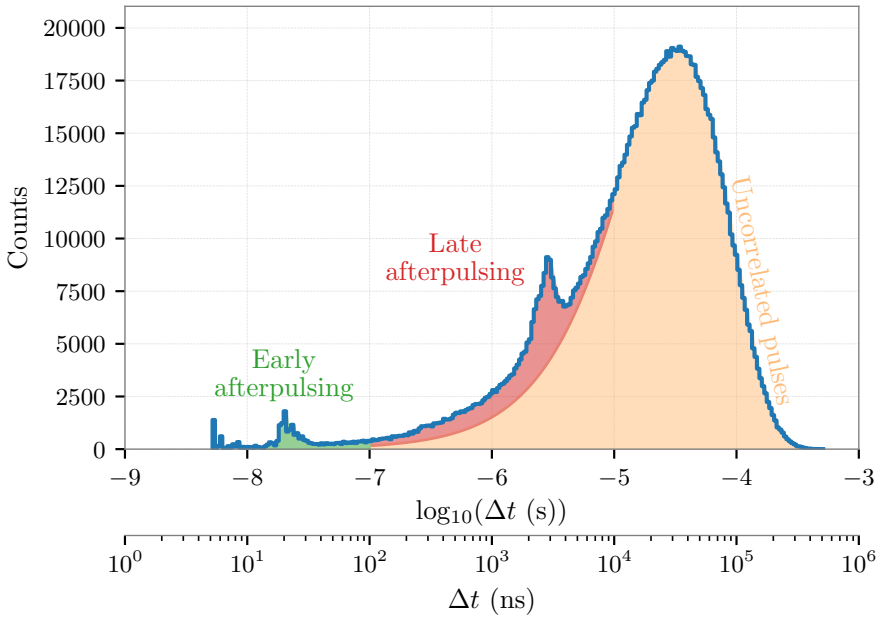

Fig. 7.3: Histogram of the logarithm of the time between subsequent photons Δt at -50°C. The coloured areas show the respective signal domains where correlated scintillation photons are omitted for simplicity. Only pulses due to scintillation should account for the PMT rate whereas afterpulsing is corrected for via its probability. The uncorrelated background is corrected for by the background measurement from fig. 7.2.

The peaks at $\sim -7.7\log_{10}(\mathrm{s})$ and $\sim -5.5\log_{10}(\mathrm{s})$ correspond to a mean delay time of $\sim 20\,\mathrm{ns}$ for early afterpulsing and $\sim 3\,\mu\mathrm{s}$ for late afterpulsing, respectively. The combination of different Poissonian processes with respective rates results in a single broad peak of uncorrelated pulses at $\sim -4.5\log_{10}(\mathrm{s})$ (31 µs). This peak is lower for increasing temperatures since less scintillation photons are measured. As one can gather from the marked areas in the plot, the presence of afterpulsing can falsify scintillation rates significantly if overseen and thus needs to be corrected for. For this, the probabilities for both types as shown in fig. 7.4 are considered.

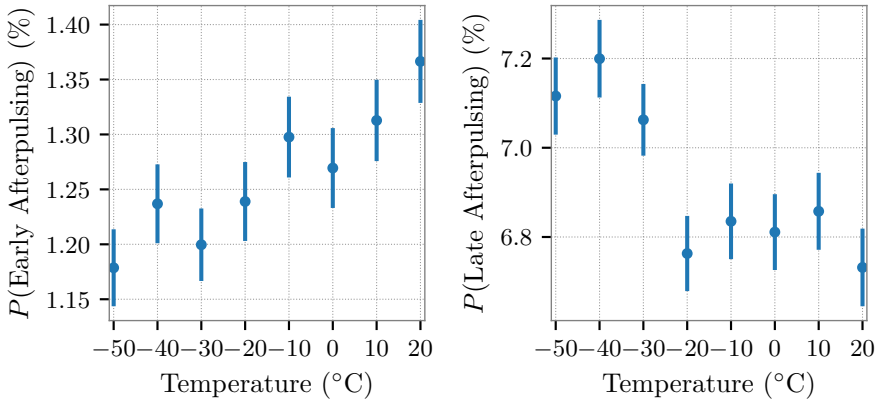

Fig. 7.4: Probability of early and late afterpulsing as a function of temperature for a nominal gain of $5 \cdot 10^6$ for the PMT used in this work as measured in [25].

For each temperature, the afterpulsing correction applied to the PMT rates is given by

$$C_{\mathrm{AP}} = 1 - P(\mathrm{AP})$$
$$\text{with} \qquad P(\mathrm{AP}) = P(\mathrm{API}) + P(\mathrm{APII}),$$

$P(\mathrm{AP})$ denoting the total afterpulsing probability by adding both individual probabilities for each temperature. The circumstance that early afterpulsing can cause late afterpulsing and vice versa is incorporated in the measurement method. Hence, the measured PMT rates are not affected for a total probability of 0 % and decrease for higher afterpulsing probabilities.

7.1.3 Count loss due to trigger

The trigger in the measurement not only rejects noise but further excludes low amplitude PMT signals below that threshold. To correct for this, the loss fraction is determined in the following.
First, the trigger needs to be expressed in terms of photoelectrons which is obtained through the following relation:

$$\mathrm{Trigger}_{\mathrm{phe}} = \frac{\mathrm{Trigger}_{\mathrm{amp}}}{\mathrm{Mean}_{\mathrm{amp}}}.$$

The threshold $\mathrm{Trigger}_{\mathrm{amp}}$ in units of mV as set in the measurement is divided by the mean of all recorded amplitudes $\mathrm{Mean}_{\mathrm{amp}}$, as shown in fig. 7.5. This threshold in units of photoelectrons can then be compared to the corresponding charge histogram since the PMT is always operated at nominal gain. The correlation between charge and photoelectrons is

$$\mathrm{Photoelectrons} = \frac{\mathrm{Charge}}{Q_1},$$

where Q_1 stems from a charge calibration (see section 3.5). With this, the trigger threshold can also be determined in terms of electron number or charge. In the charge histogram as shown in fig. 7.6 the pedestal and low charge PMT pulses are absent due to the trigger.

For an estimate of how many low amplitude signals are lost, a measurement without trigger and noise is required which is not achievable in reality. In the charge calibration, the PMT response is approximated by Gaussians and with that, an accurate photoelectron spectrum cannot be generated for this case since negative electron numbers reaching the anode are not possible. To construct a realistic electron distribution for the nominal gain, the method described in [57] is used for which the secondary emission factors δ_i are required.
In this type of PMT there are $N = 10$ dynodes whereas the potential between the photocathode and first dynode is 3/13 of the supply voltage V and 1/13 between every other dynode. To calculate the total number of electrons reaching the anode (which corresponds

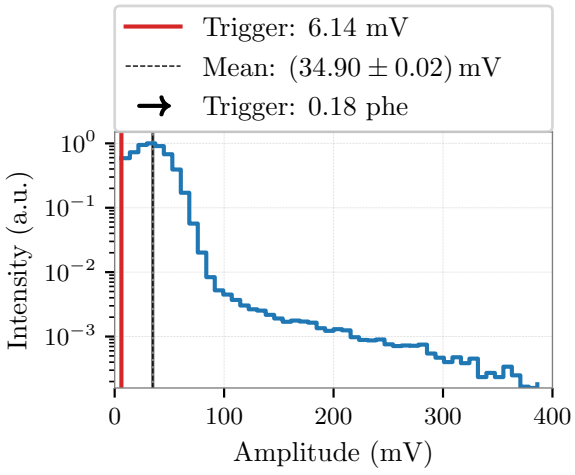

Fig. 7.5: Exemplary amplitude histogram to obtain the trigger in terms of photoelectrons. Although the trigger was set to 6 mV in the measurement, the lowest amplitude value is considered due to the oscilloscope's resolution.

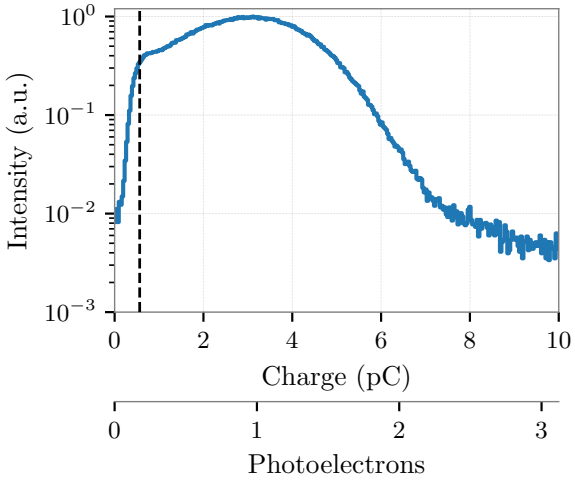

Fig. 7.6: Exemplary charge histogram to visualise the correlation between charge and photoelectrons. The black line indicates the trigger.

to the nominal gain in this case) one can apply the following relations (see eq. 3.1):

$$\delta_1 = a\left(\frac{3}{13}V\right)^k \quad \text{and} \quad \delta_n = a\left(\frac{1}{13}V\right)^k$$
$$\text{Gain} = \delta_1 \cdot (\delta_n)^{\text{N}-1}.$$

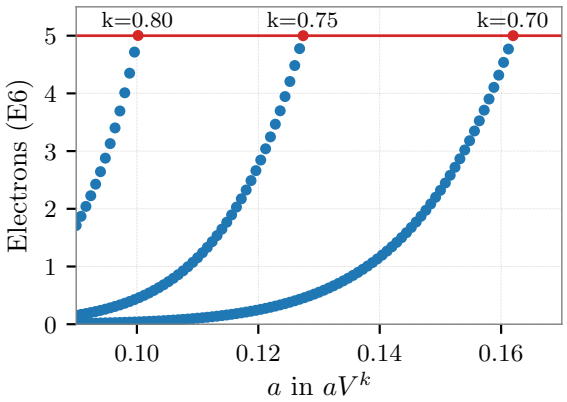

Fig. 7.7: Variation of a and k for a total number of electrons reaching the anode equating to the gain to calculate the secondary emission factors.

Both secondary emission factors can be calculated by varying the a (PMT specific constant) and k (indicating material and surface properties) to achieve an electron number equal to the nominal gain ($5 \cdot 10^6$) which is shown in fig. 7.7.
The supply voltage does not impact δ_1 or δ_n since it only scales a. A different $k \in (0.7, 0.8)$ value however varies the results from $\delta_1 \in (9.34 - 10.31)$ and $\delta_n \in (4.33 - 4.28)$, respectively. Since there is no known approach to reliably measure k and it should lie between 0.7 and 0.8 as per [21], the value of 0.75 is chosen. With these secondary emission factors δ_i, one can model the PMT response by iterating over the dynodes. The first dynode would have one incoming photoelectron and multiply it by a Poissonian with mean $\mu = \delta_1$ which would be the input for the following nine dynodes with $\mu = \delta_n$. This explicit approach however requires much computational effort which is where the analytic description as developed by [57] is considered.

The resulting total secondary electron number reaching the anode (the mean equating to the nominal gain in this case) is shown in fig. 7.8 and corresponds to a distribution without trigger and zero noise for single photoelectrons. In this, the aforementioned threshold (in units of charge) can be applied to calculate the missing portion which is getting cut out by the trigger. In every measurement with the amplifier the photoelectron-loss P_{Loss} is below 0.2 % which is considerably low, because the chosen gain is rather high and the trigger can be set relatively low due to the amplifier. The first measurement was done without the amplifier and exhibits a loss of 1 % since the trigger is set higher relative to the signal strength.

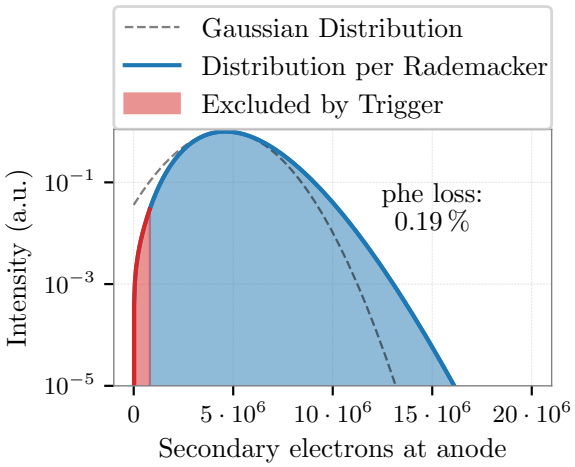

Fig. 7.8: Analytic SPE response in which the trigger is applied to calculate the photoelectron loss. The mean of this distribution lies at $5 \cdot 10^6$ and does not resemble a Gaussian process as indicated by the gray line.

The correction applied to the PMT rates is described as

$$C_{\text{loss}} = \frac{1}{(1 - P_{\text{Loss}})}$$

which raises the measured rates in case of lost photons and is passive for 0 % loss.

7.1.4 Simulated detection efficiency for different yields

For the detection efficiency of the measurements, the setup from section 7.1.1 is replicated in a Geant4 simulation as visualised in fig. 7.9.

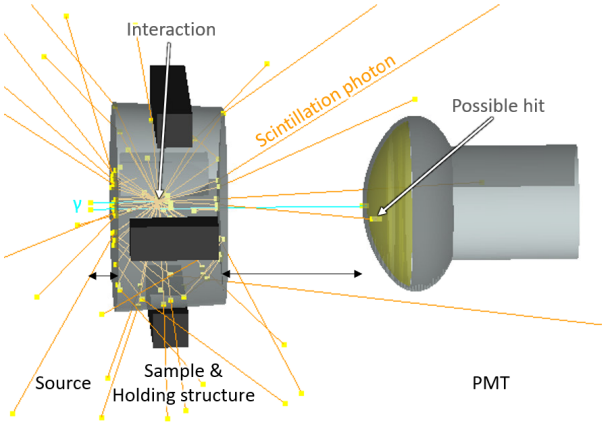

Fig. 7.9: Two exemplary γ events (blue) emitted horizontally instead of isotropic. One excites the glass sample, causing scintillation photons (orange) and the other does not interact.

For this the PMT geometry, sample dimensions, holding structure, and spacing of the three components have to be constructed within the simulation framework explained in chapter 5. For the Vitrovex glass, the optical properties are defined by the absorption length and refraction index, whereas the holding structure is implemented as a photon absorber. The 'detector' is the photocathode area that, if struck by a photon, stops it and stores the wavelength as well as hit time.
An event is a single incident γ-particle with an energy of $E_\gamma = 611.17\,\mathrm{keV}$ (^{137}Cs source) emitted isotropically, totalling 100 million individual events per simulation. Depending on the yield of the sample (which is varied between simulations), γ-particle might cause scintillation photons varying in quantity, depending on the deposited energy onto the electron, with the distinct wavelength distribution as measured in chapter 6. Note that the measured scintillation spectrum does not include transmission, reflection or similar effects occurring within the glass sample and represents the scintillation spectrum emitted at the surface. These photons eventually strike the photocathode area where a PMT hit is denoted if it passes a quantum efficiency filter corresponding to the measured QE of the PMT.
Each setup is simulated for yields in range of $0 - 500\,\mathrm{MeV}^{-1}$ and temperatures from -15 °C to -50 °C with the lifetime variance from [10]. However, the temperature alterations for the lifetime was found to be negligible. The relative deviation from the mean for all simulated temperatures is $< 0.1\,\%$ across all yields.
From each simulation the number of detected photons is saved, whereas the

$$\textbf{hit probability } H(Y) = \frac{\text{Detected photons} - \text{Hits within dead time}}{\text{Number of Events}} \tag{7.1}$$

for each simulation with the given parameter set is calculated. Thus, the simulation gives a reference for the expected number of detected photons if the scintillation yield of the glass sample is varied which can consequentially be related to the measurements once the activity of the source is known.

An exemplary result is shown in fig. 7.10. For a sample electron yield of $500\,\mathrm{MeV}^{-1}$, the PMT would detect a hit $6.41^{+0.34}_{-0.30}\,\%$ of the time after a γ-particle emission. The uncertainties are asymmetric as the amount of detected hits increased non-linearly towards denser setups due to the geometrical efficiency (solid angle covered for point sources). For a yield of $0\,\mathrm{MeV}^{-1}$ all resulting PMT hits originate from Cherenkov photons caused by electrons after gamma interactions which is a constant contribution within all simulations

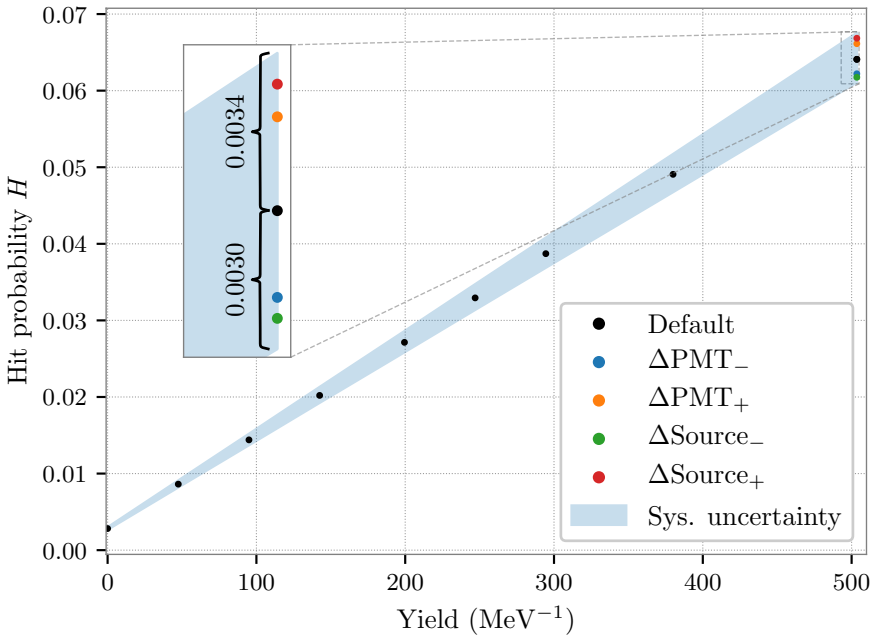

Fig. 7.10: The simulated hit probability of the setup (as manually measured) is shown in black whereas the systematic uncertainty stemming from the spacing measurement is overlayed in blue. The magnified subplot is to demonstrate that the uncertainties are asymmetric.

for each setup. As the yield (number of photons emitted per deposited energy) rises, the number of expected PMT hits scale linearly with it.
Since the distances from the source to the sample and from the sample to the PMT are measured manually, the uncertainties have to be considered. Simulations however give an exact result apart from negligible statistical fluctuations for the large number of events. This distance measurement poses the largest uncertainty since the geometric acceptance will increase or decrease the amount of photons reaching the photocathode significantly. Otherwise, slight variations in thickness between the samples, source geometry (circle or point source), or indented sample structures were found to be negligible.
In order to establish uncertainties from the simulations, the spacings are individually varied for the four possible variations ($\pm\Delta_{\mathrm{PMT}}$ and $\pm\Delta_{\mathrm{Source}}$). The case of uncertainty will be noted as *denser* (ΔH_d) or *further* (ΔH_f), whereas the differences to the *default* setup H_0 is combined via Gaussian error propagation for both the source and the PMT:

$$\Delta H_{\mathrm{d,f}} = \sqrt{(H_0 - H_{\Delta\mathrm{PMT}})^2 + (H_0 - H_{\Delta\mathrm{Source}})^2}. \tag{7.2}$$

Here, the indices d and f classify the case of uncertainty (PMT and source closer or further from the sample) which has to be handled separately, since the uncertainties are asymmetric.
Since the simulation scales linearly with the yield, this asymmetric uncertainty can be applied as two separate percentages to any data point. Thus, the uncertainty percentage for both cases is calculated for a yield of 500 MeV^{-1}, saving the computational effort for each simulated yield.

Whether this approximation represents the uncertainty accurately is examined with a correct error estimation which will be explained in the following. Instead of simulating the four extreme cases exclusively and combining them via error propagation, the spacing of both PMT and source to the sample is set by two separate random Gaussian distributions, in which the spread σ is equal to the previous uncertainties and the mean μ corresponds to the default setup. The distribution and simulation results of 70000 randomised spacings with 1 million events each are shown in figs. 7.11 and 7.12.

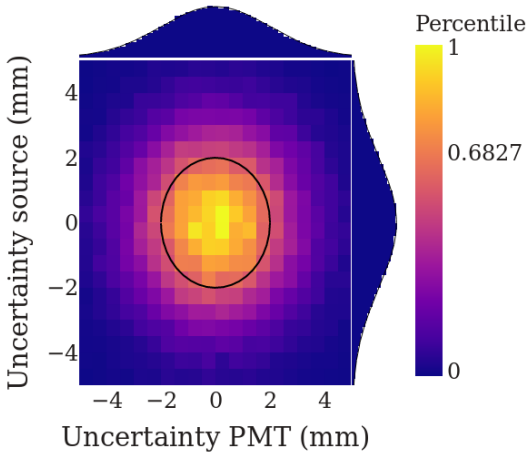

Fig. 7.11: Spacing distribution of the simulated setups where the uncertainties are varied with two random Gaussians of spread $\sigma = 2\,\mathrm{mm}$ as indicated by the black circle and the 68.27 percentile. The default setup equates to the point $(0, 0)$.

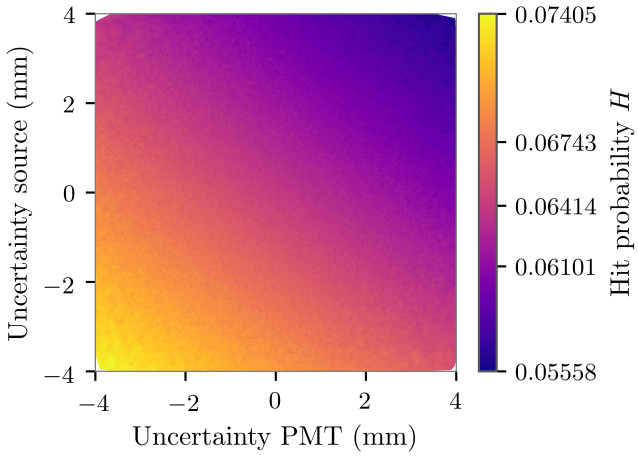

Fig. 7.12: Simulated hit probability for the randomised source and PMT positions. For denser setups more PMT hits are generated (yellow) and less hits (blue) if the components are set further apart.

In order to gauge a sensible result interval from this data set, the most likely value of H is determined by fitting a Gaussian distribution to the frequency of simulation results as shown in fig. 7.13. As the results are distributed asymmetrically, the logarithm $\log(H)$ is used for fitting and then exponentiated ($e^{\log(H)} = H$) again for the corresponding values μ and σ, which establish the confidence interval.

To compare the correct results of this method with the one described above, the cumulative distribution function $\mathrm{CDF}(H)$ as shown in fig. 7.14 is used. Here, the most likely value with the respective $1\,\sigma$ confidence interval is compared to the uncertainty interval from the previous method. The accompanying values are listed in table 7.1.

Table 7.1: Mean and confidence interval of the simulated hit probability H for both described methods. The exact values are not relevant for the discussion at hand but rather that both approaches generate very similar results.

Method	$\mu - \sigma$	μ	$\mu + \sigma$
I. Gaussian error propagation	0.06109	0.06409	0.06752
II. Randomized spacing	0.06101	0.06414	0.06743
Relative deviation	0.13 %	0.08 %	0.13 %

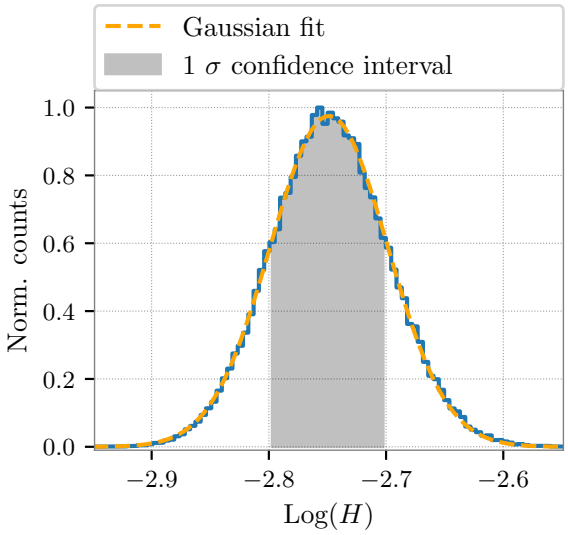

Fig. 7.13: Histogram of simulation results H for the spacing distribution from above. The Gaussian fit (orange) of the logarithmic data determines the most likely value and the 1σ confidence interval after exponentiation.

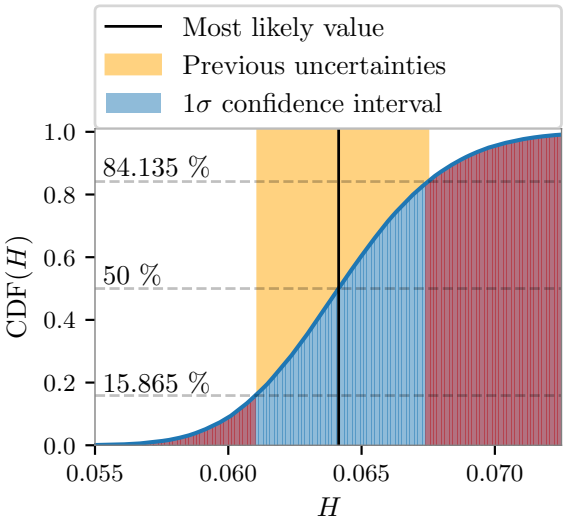

Fig. 7.14: Cumulative distribution function of the simulation results (blue line). The most likely value (black) constructs the 1σ confidence interval (blue area) and is compared to the previous uncertainties (orange) which is slightly shifted towards higher values.

In total, the simpler method described above provides an almost identical result and will henceforth be used as an approximation. The vast additional computational and time effort does not justify the need for slightly higher precision, given that the uncertainties were chosen conservatively nonetheless.

7.2 Determining the source activity

7.2.1 Gamma spectroscopy

To calculate expected PMT rates from the simulation in section 7.1.4, the activity of the source has to be known for time information.
To measure the activity of the gamma source, a germanium-sodium semiconductor detector is used to record an energy spectrum. Incident γ-radiation produces an ionising electron in the p-n junction of the semiconductor which produces electron-hole-pairs proportional to its energy. These charge carriers are collected, amplified, and read out by a multi-channel analyser where the channels correspond to different energies in which the amount of detected signals are saved. The counts of each channel are divided by the time of measurement for a detector rate and an exemplary resulting spectrum is shown in fig. 7.15. The full energy peak (FEP) corresponds to events resulting from total absorption of the γ-particle. Impulses of lower energies than E_γ belong to the Compton continuum. The detector rate due to full gamma absorption can be calculated by integrating the FEP. For a more exact determination of this area, the detector rate from events with slightly lower energies than the FEP are fitted with a linear function and subtracted from the net peak area. The obtained FEP area is shown in the magnification of fig. 7.15.

This measurement is performed for eleven different setups whilst the horizontal distance of the source centred to the detector is varied.[6]

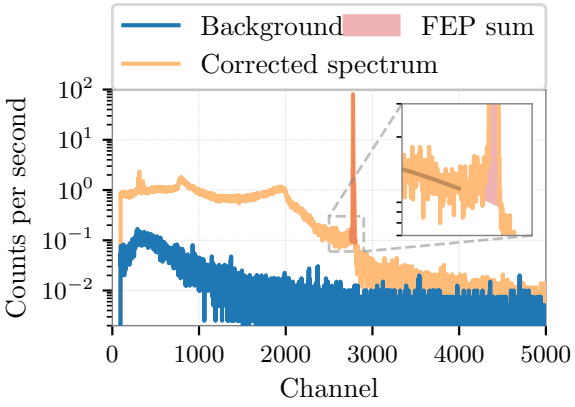

Fig. 7.15: Evaluation of the detector rate from ^{137}Cs gamma spectroscopy. The background (blue) is subtracted from the measurement and the FEP area (red) is calculated from the corrected data (orange) up to the linear fit (gray).

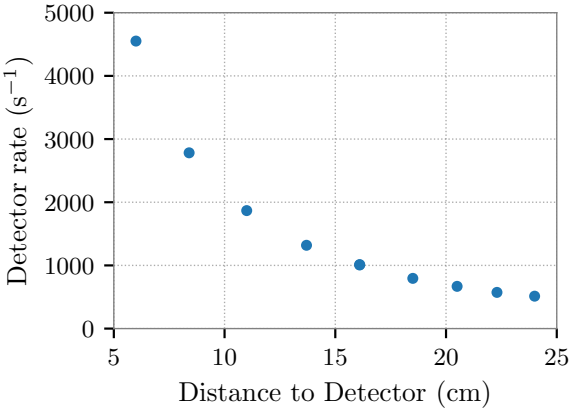

Fig. 7.16: Detector rate for gamma spectroscopy of different distances of the source to the detector. The error bars consider the statistical uncertainty as well as the error stemming from the fit, but are smaller than the size of the markers.

The detector rates fall with increasing distances of the source as seen in fig. 7.16. The absolute activity of the source is calculated by $A = R/\epsilon$, where R is the detector rate and ϵ the detection efficiency for each distance respectively.

7.2.2 Simulation for the detector efficiency

Obtaining the detector efficiency dependant on the setup, i.e. distance of the γ-source to detector in this case, is accomplished by a simulation.
The Geant4 simulation as visualised in fig. 7.17 used for this was written by Volker Hannen and resembles the detector used in section 7.2.1. For a total of 100 million events, γ-particles with $E_\gamma = 611.7\,\mathrm{keV}$ are emitted isotropically from the source distances as presented in fig. 7.16. The simulation output is a spectrum in terms of energy (fig. 7.18) which is compared to the measurement.

The only noticeable difference between the spectra is the effect of lead shielding close to the detector resulting in X-rays and stronger Compton backscattering in lower energy domains, which are absent in the simulation, but has no effect on the calculations. Furthermore, the simulated FEP is smeared by a Gaussian with a smaller spread than in the measurement. To calculate the respective detector efficiency, the simulated FEP area is determined like previously, but divided by the total number of events instead of measuring time.

[6]The measurements are performed with different shaping times to keep the dead time percentage lower than ten percent. Some distances are repeated with different integration times, yielding the same result for verification.

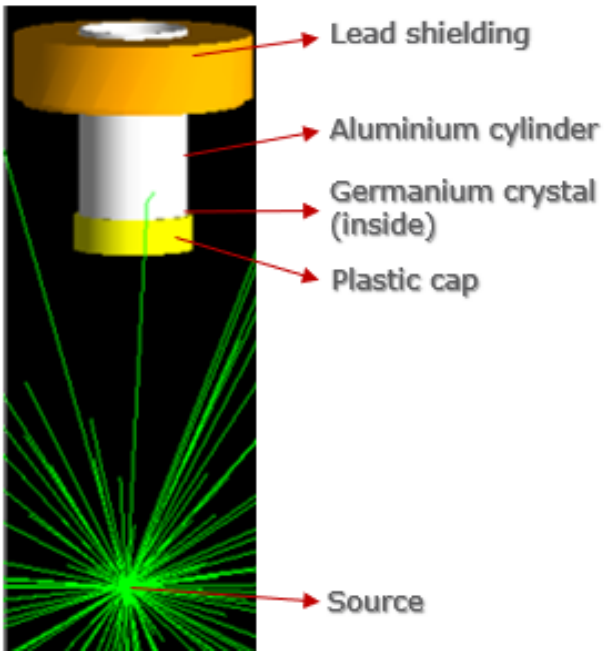

Fig. 7.17: Cumulative output of 100 γ events (green) for the simulated detector rate of this setup.

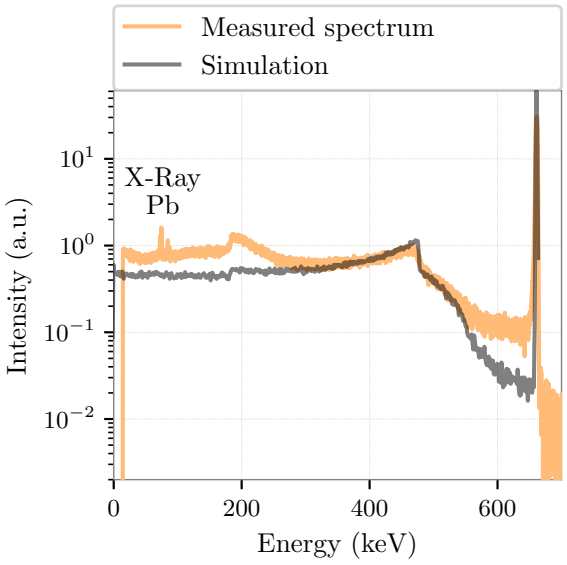

Fig. 7.18: Simulation result (gray) compared to the previous measurement (orange). Note that the graphs are just roughly scaled to each other, since an energy calibration of the measurement was not necessary whilst the simulation generates the distribution in terms of energy.

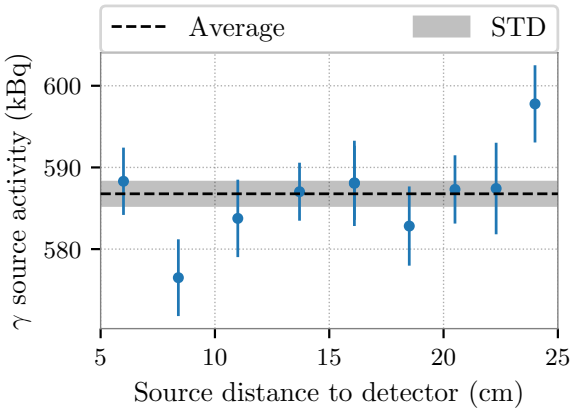

Fig. 7.19: Determined activities for the ^{137}Cs source from several measurements.

The activity is calculated by dividing the measured detector rate with the detector efficiency for each respective distance. The results are shown in fig. 7.19 with a mean of $586.8 \pm 1.4\,\mathrm{kBq}$.
The exact (inner) geometry of the source is not known, since the ^{137}Cs is shielded by an electron absorber. Hence, the distances from the detector to the source are only measurable up to this shielding. However, the distance from the source to the sample is measured in such way in section 7.1.1 as well and the determined activity thus represents the rate of decays for a measured distance of 0 mm. It is simply to note that the actual activity of the radioactive material inside of the shielding would be slightly higher.

7.3 Calculating the electron yield

To obtain the scintillation yield, the temperature dependant measured PMT rates are compared to expected rates R_{Exp} stemming from the simulation, activity of the source and PMT related corrections factors. One can forthwith calculate expected PMT rates by

$$R_{\text{Exp}} = \frac{H(Y) \cdot A}{C_{\text{Loss}} \cdot C_{\text{AP}}}. \tag{7.3}$$

Here, $H(Y)$ denotes the simulated PMT hit probability with varying scintillation yield from section 7.1.4 and A the activity which was obtained in section 7.2.2. It is irrelevant whether the measured rates from section 7.1.1 are decreased or the expected rates are increased by the corrections C.
The simulated rates are calculated for each yield by eq. 7.3 which are then compared to the temperature dependant measured rates (see fig. 7.21). For each temperature the intersection point in terms of scintillation yield of the simulated rates (linear) and the measured rates (constant) is determined as shown in fig. 7.20.

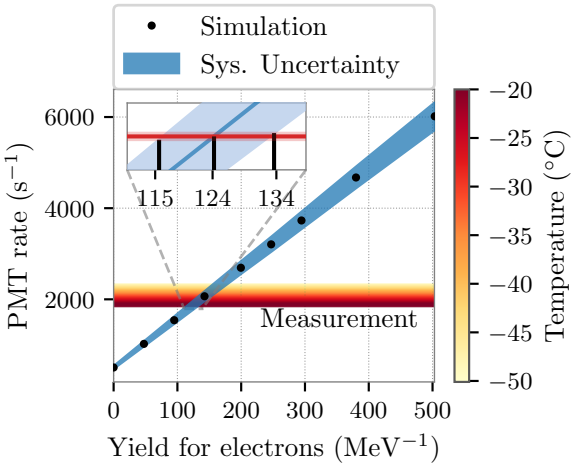

Fig. 7.20: Simulated PMT rate (blue) from eq. 7.3 compared to the measured rate (independent of the abscissa). The asymmetric systematic uncertainty of the simulation stemming from the manual distance measurement in combination with the statistical uncertainty of the measurement results in the margin of error for the yield.

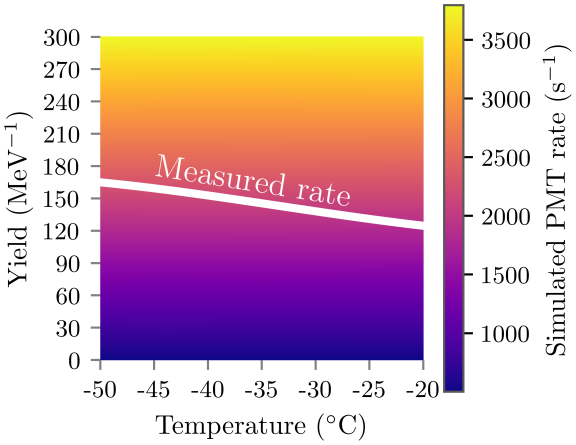

Fig. 7.21: Interpolated expected PMT rate in the ranges of measured temperatures and simulated yields. The measured rate is overlaid in white for classification.

As indicated before, the entire process is repeated for six different setups as listed in table 7.2 composed of different samples and spacings. The determined scintillation yield for each setup is shown in fig. 7.22 whereas the values are presented in table 7.3.

Table 7.2: Parametrisation of the different measured setups for the electron yield necessary for the Geant4 detector construction. The uncertainty stems from manual measuring and samples with the suffix * are from an older manufacturing batch.

		Spacings (mm)	
Setup	Sample	Source - Sample	Sample - PMT
1	2	74 ± 3	89 ± 3
2	1	1.5 ± 0.5	33 ± 1.5
3	1	10.5 ± 1.5	63 ± 2
4	3*	13.5 ± 2	77.5 ± 2
5	4*	13 ± 2	79.5 ± 2
6	1	69 ± 2.5	116 ± 4

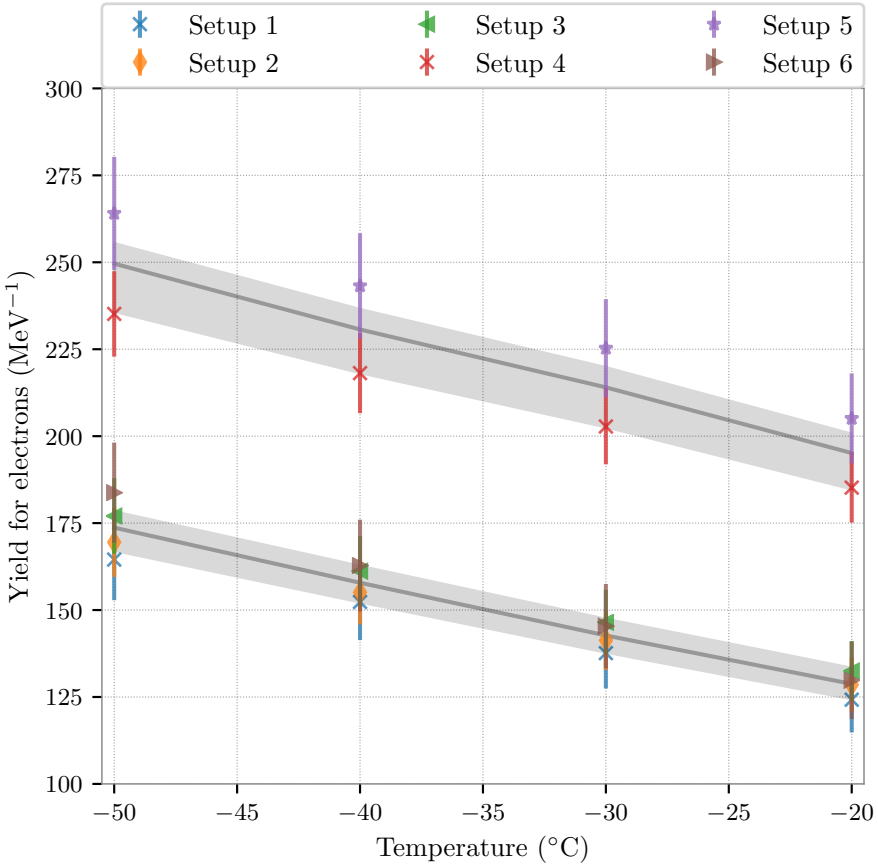

Fig. 7.22: Comparison of the electron scintillation yield from all setups as listed in table 7.2. The weighted mean (gray) is taken for all samples of the respective manufacturing batch.

All sample and setup variations show a similar linear behaviour regarding the temperature slopes of the electron scintillation yield.
Sample 1 was measured for three different PMT-source spacings that generally result in the same scintillation yield within the margin of error. The slight vertical shift between setups may be explained by minor differences in orientation or alignment of all three components (source, sample, PMT), since the setup has to be manually reassembled between each measurement. Nonetheless, this shows that the method used produces sensible and reproducible results.

Sample 2 matches these results as slight alterations can be explained by trapped air bubbles in the glass and the fact that the angle between the cutting planes slightly varies for each sample. This impacts the measurement but cannot be simulated accurately since the samples show very minor differences.
Additionally, two samples from an older manufacturing batch (2015) were investigated as well where one can clearly see a discrepancy compared to the yields of the samples from 2018. This could be traced back to production influences and small variations in composition of the glass which will be discussed further in chapter 9. Since γ-particles discretely interact within the entire sample volume, expected differences of the surfaces do not contribute much to this. A shift between both samples from the 2015 batch can once again result from minor sample variations (trapped air bubbles and uneven cuts) or inaccurate manual assembly.

Table 7.3: Electron yields (MeV^{-1}) for all setups for temperatures from -50°C to -20°C. The values state the error margin whereas the mean considers the respective manufacturing batches, the asterisk denoting samples from 2015.

	-50°C	-40°C	-30°C	-20°C
1	$164.5^{+11.7}_{-10.7}$	$152.3^{+11.0}_{-10.1}$	$137.6^{+10.2}_{-9.3}$	$124.2^{+9.4}_{-8.6}$
2	$169.5^{+10.0}_{-9.6}$	$155.1^{+9.2}_{-8.9}$	$141.3^{+8.5}_{-8.3}$	$128.5^{+7.9}_{-7.7}$
3	$177.0^{+10.9}_{-11.3}$	$161.2^{+10.1}_{-10.4}$	$146.5^{+9.3}_{-9.6}$	$132.5^{+8.6}_{-8.8}$
4*	$235.2^{+12.3}_{-12.5}$	$218.1^{+11.5}_{-11.7}$	$202.8^{+10.9}_{-11.0}$	$185.2^{+10.1}_{-10.1}$
5*	$264.1^{+16.3}_{-15.9}$	$243.2^{+15.2}_{-14.7}$	$225.3^{+14.1}_{-13.7}$	$205.1^{+12.9}_{-12.7}$
6	$183.7^{+14.4}_{-13.6}$	$162.8^{+13.2}_{-12.4}$	$145.4^{+12.1}_{-11.4}$	$129.8^{+11.1}_{-10.5}$
Mean	$172.6^{+5.7}_{-5.5}$	$157.4^{+5.3}_{-5.1}$	$142.5^{+4.9}_{-4.7}$	$128.8^{+4.5}_{-4.4}$
Mean*	$245.7^{+9.8}_{-9.8}$	$227.3^{+9.2}_{-9.1}$	$211.2^{+8.6}_{-8.6}$	$192.7^{+7.9}_{-7.9}$

7.4 Impact of lifetimes

The third and last scintillation parameter – the lifetime – has not been investigated yet, despite being implemented in the simulation. The lifetime determines the mean time scale of de-excitations and is split into three temperature dependant exponential decay components. For a temperature of $-50\,°C$ the components correspond to 377 ns, 2985 ns, and 3541 ns respectively [10]. The dead time of the measurements is set to 20 ns and thus it is highly unlikely that two scintillation photons are detected at the same time. Since these lifetimes are measured only for alpha radiation there is a possibility that the lifetime following electron excitation is faster then assumed. If the majority of the de-excitations were to occur in tens of ns, the measured PMT rates would not represent the amount of de-excitations accurately and thus the calculated yield would reflect a lower value than in reality. Whenever the timing of multiple photons occurs within the dead time, they are counted as one pulse with higher charge.

To address and resolve this potential issue, the simulation from section 7.1.4 is re-done with an electron yield of $172.6\,\mathrm{MeV}^{-1}$ for extreme cases such that the lifetime is a single fast exponential decay with varying time from 20 ns to 10 µs for 10 million events each. The simulation now additionally saves the time offset of each detected photon within one event. The timing of the first photon hit is irrelevant and set to 0 ns. The time offset Δt of following photons however is important if it is smaller than the dead time which would result in one multi photon pulse in reality, thus raising the charge but not the rate. In practice however, scintillation photons rarely cause multi photoelectron signals as seen in fig. 7.6. For comparison, a photoelectron histogram (fig. 7.23) can be constructed using the simulation data whenever subsequent scintillation photon timing falls below the dead time. To obtain a comparable charge histogram from simulations, the integer results are smeared with a Gaussian distribution with a spread of $\sigma = 0.39\sqrt{n}$ which was obtained from calibration of the PMT (fitted with eq. 3.3).

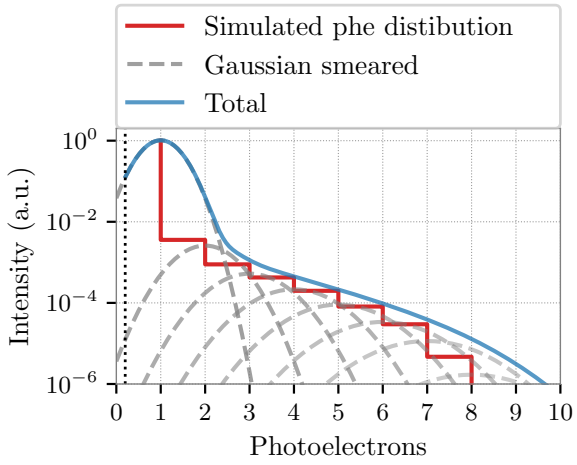

Fig. 7.23: Simulated photoelectron distribution for a lifetime with a single exponential decay exemplarily shown for 10 µs. The photoelectron number accumulates whenever a following photon falls within the dead time of the initial one. The total signal below the trigger threshold is excluded.

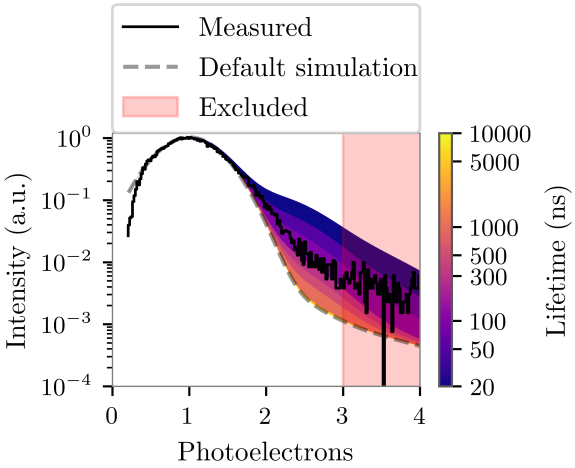

Fig. 7.24: Simulated photoelectron distributions for different lifetimes (coloured) compared to the measured spectrum (black). The gray line indicates the photoelectron distribution obtained from simulations as implemented in the previous calculations where three decay components are assumed.

Further, the data below the 0.2 phe trigger threshold from the measurement is excluded as indicated in the plot. For this fixed scintillation yield, the photoelectron mean raises towards shorter lifetimes. These photoelectron spectra can then be compared to measurement results as shown in fig. 7.24 since multi photon information is stored in charges to estimate the lowest possible lifetime.
The measurement however includes afterpulsing which raises the number of pulses with multiple photoelectrons. The mean photoelectron number from the measurement is (1.075 ± 0.001) phe for phe < 3. With this, one can estimate that the lifetime would lie roughly around 100 ns in this worst case scenario, which only corresponds to 0.32 % of lost photons.

The mean charge however scales not only with shorter lifetimes, but also with increasing scintillation yield. Hence, the portion of photon loss due to measurement dead time

is constructed numerically by varying both, the mean lifetime of transitions τ and the average number of detected scintillation photons per radioactive decay μ which is of Poissonian nature. The lifetime τ is the decay constant of an exponential decay $\propto \exp(-t/\tau)$ (see section 4.3) where the probability density function (PDF) is given by $1/\tau \exp(-t/\tau)$, t denoting a time. For each of the $n = P(\mu) = \frac{\mu}{k!} \exp(-\mu)$ emitted photons, a random exponential from the PDF is drawn, giving its time of emission t which is shown in fig. 7.25.

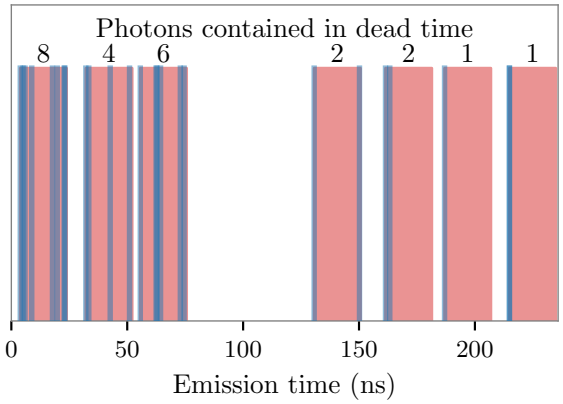

Fig. 7.25: Randomised emission time t of photons (blue lines) for $\mu = 30$ and $\tau = 50\,\text{ns}$. The dead time is indicated in red. In this example, there are $m = 7$ pulses with M_i noted in the plot.

If the timing between subsequent photons Δt falls below the dead time of 20 ns, they are counted in a single pulse with M photons. Until the last emitted scintillation photon produced by the decay, m pulses exist with respective photon number. From the these quantities, one can calculate the mean photoelectrons and signal loss by:

$$\text{Mean photoelectrons} = \frac{\sum_{i=1}^{m} M_i}{m}$$

$$\text{Photon loss} = \frac{n - m}{n}$$

which results in a mean of 1 photoelectron and 0 % loss for $M_i = 1$ $(n = m)$ and increases for $M_i > 1$ $(n > m)$. For zero emissions $(n = 0)$, the decay is not measurable and thus excluded. This calculation is averaged from 100 000 iterations for lifetimes $\tau \in (10^{-9}, 10^{-6})$ and average detected photons per decay $\mu \in (0.1, 10)$. The results are shown in fig. 7.26 which shows the mean photoelectron number and correlated loss portion in dependence of the τ and μ.

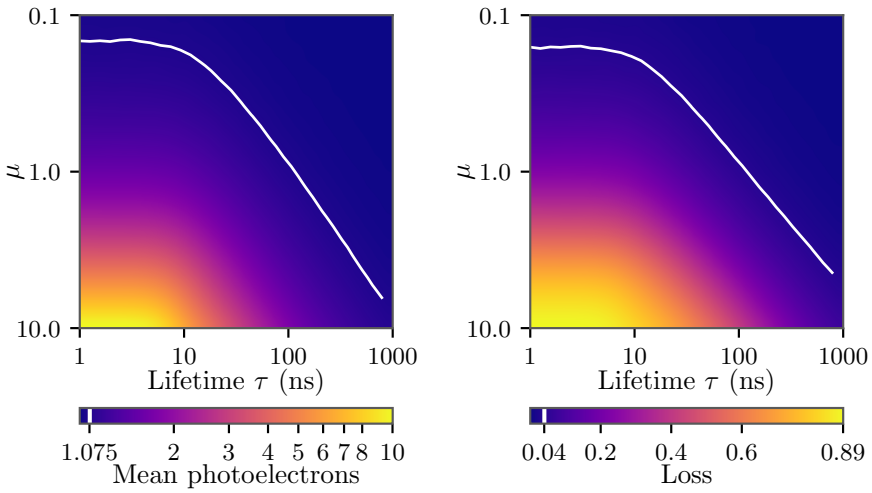

Fig. 7.26: Interpolated results for the calculations as described in the text. The mean photoelectron number from the measurement is overlaid in white and indicates the expected loss. The mean photoelectrons (left) and the photon loss (right) scale non-linearly which is why both plots are shown.

The loss and photoelectron mean are correlated non-linearly and thus the loss will vary for different lifetimes. The loss averaged from different lifetimes lies around $(4.0 \pm 1.2)\,\%$ in this worst case scenario assuming a single, quick scintillation lifetime for electron excitation.
Hence, the problem that potential low lifetimes from electron excitation in respect to the measurement dead time could lessen the measured PMT rates is negligible. However, the scintillation lifetime in glasses, which are comprised of many compounds, is much more complex than assumed here and should be measured regardless.

8 Scintillation yield for alpha particles

This chapter will determine the scintillation yield of the Vitrovex samples for alpha excitation. Although the alpha yield is determined in [10], it is essential to incorporate the electron yield into the simulation since ionisation- and δ-electrons from interaction of the alpha particle are produced in the glass. The only differences in comparison to acquiring the electron yield are the simulation and that the background rate mostly correspond to the dark rate of the PMT, since every α-particle is absorbed by the sample. Hence, the process of determining the alpha yield will not be shown in great detail whereas solely the main differences to chapter 7 will be explained.

8.1 Activity of the alpha source

To calculate the yield, the activity of the radioactive source has to be measured as done in chapter 7. The chosen alpha source is ^{241}Am and the corresponding decay scheme is illustrated in fig. 8.1.

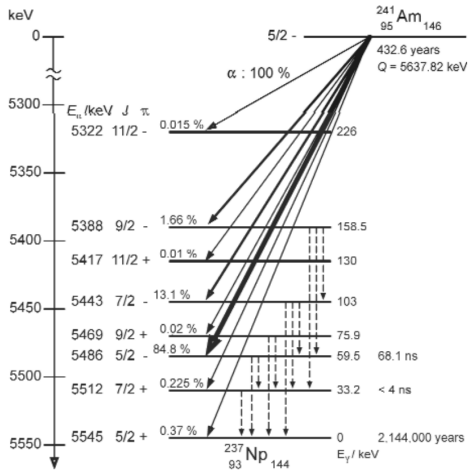

Fig. 8.1: ^{241}Am decay scheme showing possible transitions. Figure taken from [58].

This isotope has a Q-value of 5637.82 keV and can decay into eight different energy levels in comparison to the mono-energetic ^{137}Cs. The excited states decay via γ-rays until the ground state of ^{237}Np is reached. All particles with their respective energies have to be implemented in the yield simulation. The decay product ^{237}Np has a half life of $\lambda = 2.144 \cdot 10^6$ years and is therefore not taken into consideration meaning that no decay chain is assumed for simplicity.

To measure the absolute activity of the source, an alpha spectrometer is used which is similar to the setup utilised for gamma spectroscopy (section 7.2.1). The metal plate with ^{241}Am on its surface is placed in front of a semiconductor which outputs a voltage signal proportional to the deposited energy. To avoid energy loss from interactions with air molecules, the source and detector are located in a vacuum chamber with a pressure $< 10^{-7}$ bar. The signal is amplified and fed into an oscilloscope from which the rate is derived.

As before, the source is placed at different distances from the detector by using spacers where the detection efficiency has to be simulated for each case. An exemplary simulated setup is shown in fig. 8.2 in which the total number and energy of α particles striking the detection volume are saved. Electrons and gammas have low energies and do not cause strong enough signals in the semiconductor and are thus not counted in the simulation as well. Furthermore, the isotope distribution on the surface is estimated by using a circular beam profile with varying radii $R \in [0, 12]$ mm. The simulation output is the same as before, yielding the detection efficiency $\eta = \frac{\text{Detector hits}}{\text{Number of events}}$.

To compare the measured detector rates with the simulated detection efficiency, the relative change in intensity from all distances d is considered. The measured detector rate and the simulated detector efficiency at a given distance N_d is divided by the mean $\overline{N}$ from all distances as shown in fig. 8.3. The deviations from the respective mean (and the corresponding slope) should be equal for the measurement and a simulation with a realistic isotope distribution.

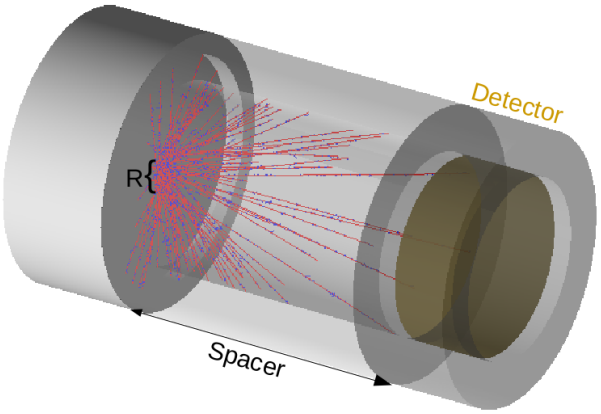

Fig. 8.2: Visualisation of one of the setups to obtain the detector efficiency η. Alpha particles (red) are emitted isotropically from a circular disc with radius R and are counted if they strike the detector volume (gold). Electrons (blue) and gammas (not shown) are not counted due to their low energy.

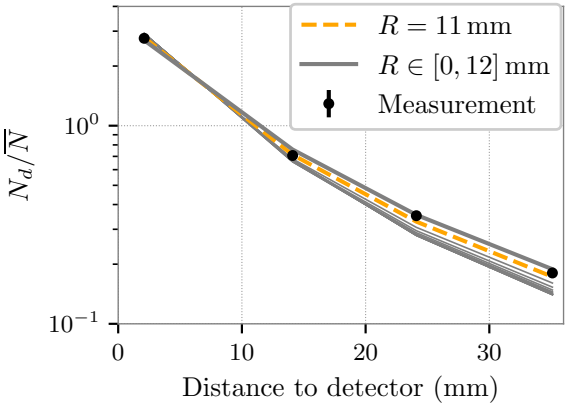

Fig. 8.3: Comparison of simulations with different radii (plotted as lines for clarity) with measurements (points) by calculating the respective relative efficiency variation $N_d/\overline{N}$ (see text) for different distances to the semiconductor. The uncertainties are smaller than the markers and the simulations are only valid for the four measured distances.

The absolute activity is obtained by division, with $A = \frac{\mathrm{Rate}}{\eta}$, where η best coincides with the measurement for $R = 11\,\mathrm{mm}$ as shown in fig. 8.3. The activity calculated from the four distances is shown in fig. 8.4 with the mean corresponding to $(2358 \pm 20)\,\mathrm{Bq}$.
The activity was measured at $(2834 \pm 81)\,\mathrm{Bq}$ in 2017 with an isotope distribution estimation of $R = 9.61\,\mathrm{mm}$ [10]. The decrease in activity is lower than expected from the half life decay of americium and could be explained by abrasion of radioactive material if the source was not handled carefully in the time frame between both measurements.

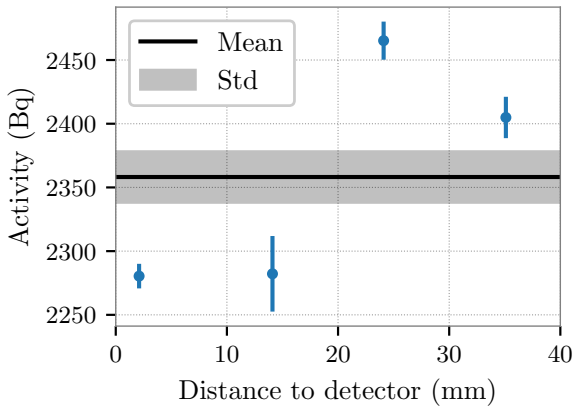

Fig. 8.4: Absolute activity of the ^{241}Am source resulting from different distances from the detector.

8.2 Determining the alpha yield

For the alpha yield, the emission of scintillation photons is again quantified by PMT rates, where the setup is shown in fig. 8.6. The measurement is performed as in chapter 7 where the support frame is placed within a climate chamber and PMT rates are acquired by an oscilloscope.

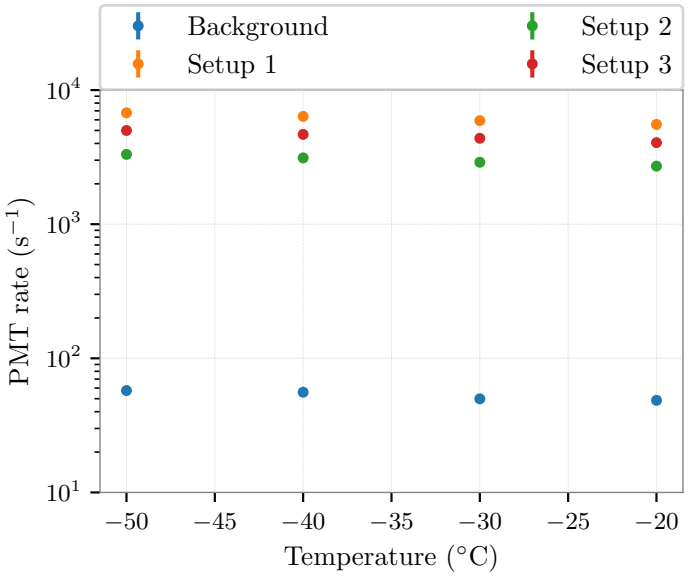

Fig. 8.5: PMT rates for different setups and background plotted against temperature. As before, the PMT rates (and the corresponding slopes) are higher if the PMT is placed closer to the scintillating sample due to the geometrical efficiency.

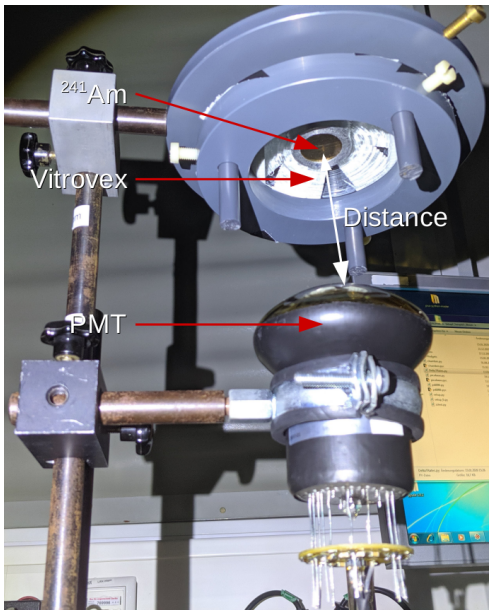

Fig. 8.6: Picture of the support frame outside of the climate chamber. The Vitrovex glass sample is fixated by a plastic holding structure and the circular ^{241}Am source is placed on top within a metal spacer.

The source is brought as close to the sample as possible to generate the greatest amount of scintillation photons stemming from the glass since this measurement cannot be performed in vacuum to avoid air scintillation. This is due to the fact that no suitable vacuum chamber to contain the setup was available which would have to be placed in the climate chamber. The source must not be in direct contact with the sample to avoid contamination and abrading the superficial radioactive material of the source. Thus the distance of $1.1 \pm 0.2\,\mathrm{mm}$ (stemming from a metal spacer) is not varied between setups. The background measurement – performed with the PMT covered – mainly corresponds to the dark rate of the PMT since every α-particle is absorbed by the $> 7\,\mathrm{mm}$ thick samples. Residual γ particles from de-excitations penetrating the sample and reaching the PMT cause a rate increase of less than $4\,\mathrm{s}^{-1}$ for the densest setup. The measured PMT rates corresponding to three differently spaced setups are shown in fig. 8.5.

Regarding the simulation, the scintillation class has to account for more than one particle yield in this case. Electrons resulting from alpha and gamma interactions in the vessel glass inherit the scintillation yield as measured in chapter 7 while the alpha yield is varied between simulation batches. Additionally, air scintillation has to be taken into

account for all particles except for gammas from de-excitations. Each scintillation yield included in the simulation is listed in table 8.1.

Table 8.1: All particle scintillation yields for air and the Vitrovex sample. The electron sample yield was measured in chapter 7 and the electron air yield stems from [59]. The alpha air yield is taken from [10] exhibiting similar results to [60] and [61] and the alpha sample yield is varied within the simulation. The temperatures correspond to the ones that the alpha lifetime was measured in.

	Yields (MeV^{-1})		
Temperature	e^- sample	e^- air	α air
-50 °C	172.63	20	17.50
-45 °C	165.00	20	18.09
-35 °C	149.96	20	18.43
-25 °C	135.69	20	18.65
-15 °C	121.98	20	18.48

The simulation as shown in fig. 8.7 resembles a replica of the measurement setup. The metal spacer encompassing the source has to be simulated in such way that it blocks particles (air scintillation photons in particular) travelling away from the sample surface. The lifetimes of photon emission induced by alpha radiation corresponds to previous measurements and does not have to be investigated as in section 7.4. The lifetime of scintillation photons stemming from air interactions is 0.5 ns [62] with the scintilation spectrum from [56].

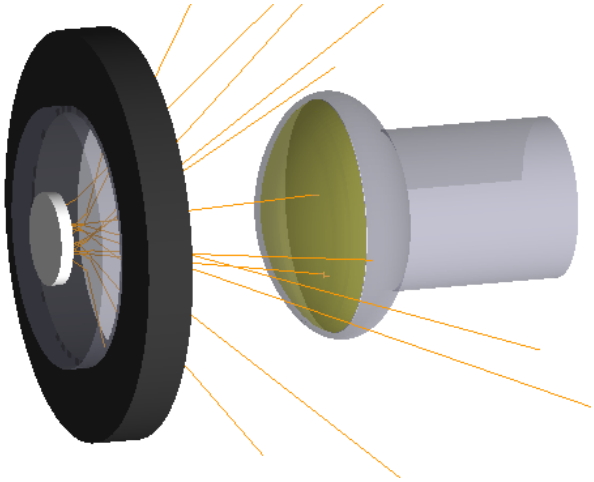

Fig. 8.7: Visualisation of the alpha yield simulation. The circular ^{241}Am source emits α-particles isotropically and is placed in the (white) spacer which acts as an absorber for all particles.

From all detected photons for an alpha yield of 100 MeV^{-1}, roughly 4.5 % originate from air scintillation, where the portion resulting from electrons is insignificant due to their low energy.
The alpha yield is measured for three different setups with two different samples from the manufacturing batch of 2018 as listed in table 8.2.

Table 8.2: Spacings and samples for the different alpha yield measurements.

		Distances (mm)	
Setup	Sample	Source - Sample	Sample - PMT
1	1	1.1 ± 0.2	45 ± 2
2	2	1.1 ± 0.2	15 ± 1
3	2	1.1 ± 0.2	22.5 ± 1.5

Due to the long time a single measurement requires the alpha yield could not further be measured for the older manufacturing batch from 2015. The results as shown in fig. 8.8

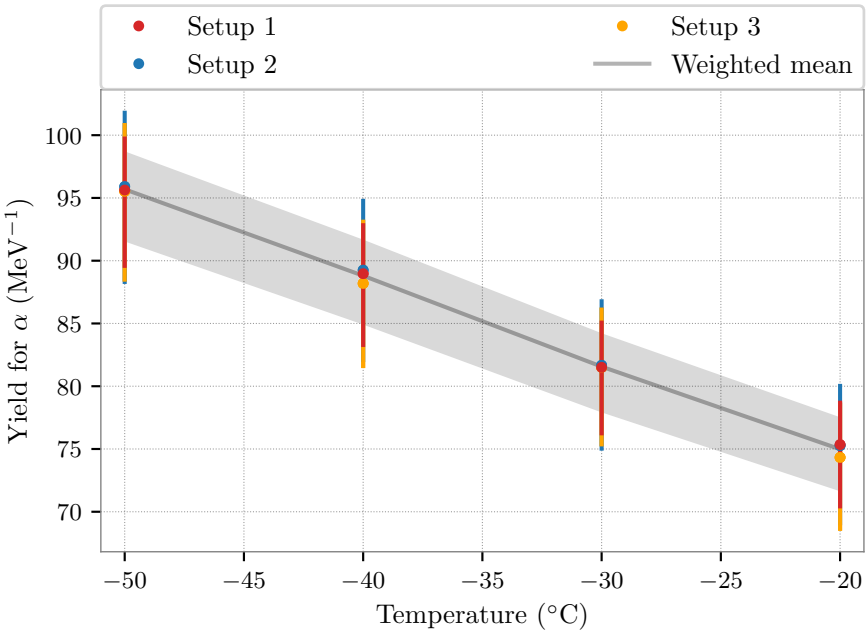

Fig. 8.8: Alpha yields in dependence of temperature for the setups as listed in table 8.2. The mean is weighted by the uncertainties of the respective data points.

are in good agreement with each other which demonstrates reproducibility and accuracy. The alpha yield as listed in table 8.3 is higher than determined in [10] as the electron yield was assumed to scale with a factor of 9.5. This causes more photons to be emitted by electron interactions, effectively lowering the α yield. The ratio of scintillation yields Y_e/Y_α is however temperature dependent as per the results of this thesis and lies between 1.6 and 1.7.

Table 8.3: Alpha yields (MeV^{-1}) for all setups for the measured temperatures from -50°C to -20°C. The asymmetric uncertainty once again arises from the fact that the detection efficiency raises non-linearly towards denser setups.

	-50°C	-40°C	-30°C	-20°C
1	$95.6^{+4.3}_{-6.2}$	$89.0^{+4.0}_{-5.8}$	$81.5^{+3.7}_{-5.4}$	$75.3^{+3.5}_{-5.1}$
2	$95.9^{+6.0}_{-7.8}$	$89.2^{+5.7}_{-7.3}$	$81.7^{+5.3}_{-6.8}$	$75.3^{+4.9}_{-6.3}$
3	$95.5^{+5.4}_{-7.2}$	$88.2^{+5.1}_{-6.7}$	$81.5^{+4.8}_{-6.3}$	$74.3^{+4.4}_{-5.8}$
Mean	$95.7^{+2.9}_{-4.0}$	$88.8^{+2.8}_{-3.8}$	$81.5^{+2.6}_{-3.5}$	$75.0^{+2.4}_{-3.3}$

9 mDOM background simulation

In this final chapter, the overall background due to scintillation and Cherenkov photons from radioactive isotopes in the vessel glass is simulated for the mDOM. The determination of this background requires an elaborate definition of scintillation parameters as established in the previous chapters. The outcome poses a final test for the veracity of the studies done in this work. For this, all scintillation properties from previous chapters are injected into the simulation framework and the measured trace amounts of isotopes in Vitrovex glass are once again listed in table 9.1.

Table 9.1: Activity per mass of three natural decay chains and ^{40}K measured in the 13 kg Vitrovex pressure vessel [10].

Decay	Specific activity (Bq/kg)
^{40}K	60.98 ± 0.86
^{238}U-Chain	4.61 ± 0.07
^{235}U-Chain	0.59 ± 0.05
^{232}Th-Chain	1.28 ± 0.05

In the simulation the mDOM[1] is constructed with all components influencing the propagation of particles and detection of photons. Thus, the pressure vessel, holding structure, reflectors, 24 PMTs, and a gel layer (optical coupler between glass and PMT to prevent reflections) are specified. All optical properties are defined by the absorption lengths and refraction indices, whereas a scattering length is additionally defined for the surrounding glacier ice.
Within the simulation, the respective decays are generated isotropically at random positions within the pressure vessel producing scintillation and Cherenkov photons as shown in fig. 9.1. The mDOM is simulated for one second at a time with the number of decays following a Poisson distribution with the activities of table 9.1. This is repeated 600 times for a total of 10 min of module background. From each photon detection, the information of which PMT was struck at a given time and the origin process of the photon is stored.

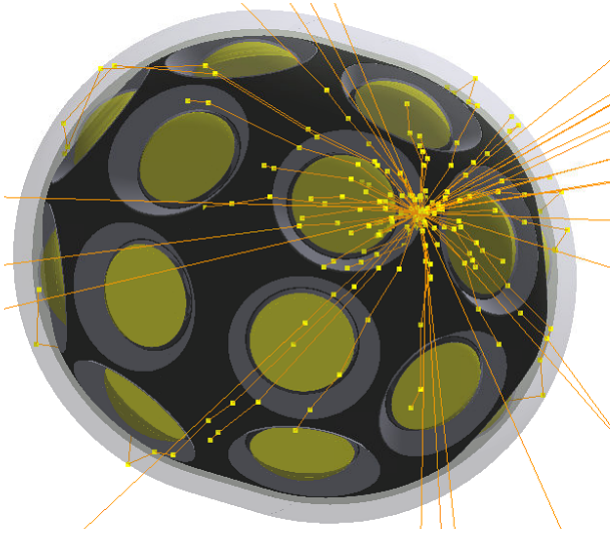

Fig. 9.1: Visualisation of the mDOM simulation exemplarily shown for a single ^{40}K decay. The decay itself is not visible since the emitted photons (orange) are studied.

[1] The dimensions correspond to the current state (as of 10.03.2020) with a glass thickness of 13.5 mm, diameter of 353 mm, a gel layer of 3.6 mm from the PMTs to the glass and a reflector angle of 50°.

The time between subsequent hits Δt from individual PMTs can once again give insight into the timing of the background processes. A $\log_{10}(\Delta t)$ histogram is shown in fig. 9.2, averaged from all 24 PMTs. Cherenkov photons of decays are produced rapidly with delays shorter than 1 ns (below $-9\log_{10}(\mathrm{s})$ in fig. 9.2) to previous photons. About 7.4 % of the photons striking the photocathode areas originate from Cherenkov processes by electrons either from β^- decays or following gamma interactions. Scintillation mostly occurs around $-6\log_{10}(\mathrm{s})$ (1 µs) which is governed by the simulated lifetimes. Uncorrelated photons from different decays cause a Poissonian peak at about $-2\log_{10}(\mathrm{s})$ (10 ms). The average background rate of individual PMTs is $(270.37 \pm 0.52)\,\mathrm{s}^{-1}$ at −35 °C.

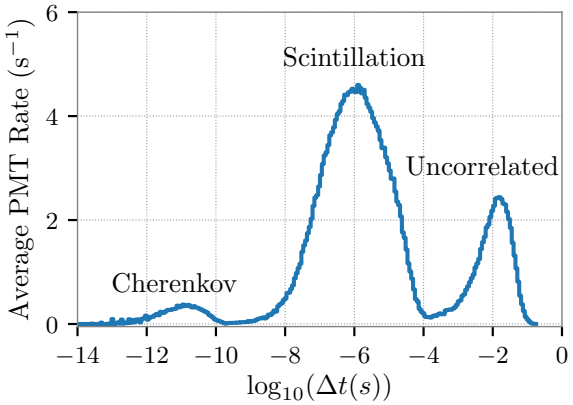

Fig. 9.2: Average mDOM PMT background rate at −35 °C represented in a $\log_{10}(\mathrm{s})$ histogram to better separate background processes (see section 7.1.2). The rate in this plot scales with the number of bins (250 in the case).

This however assumes an instantaneous PMT response corresponding to a dead time i.e. pulse resolution of 0 ns which is not achievable in reality due to the PMT timing resolution and resolution for the data acquisition system. Hence, the average PMT rate is simulated for different dead times in which subsequent hits falling below this threshold cannot be separated to estimate the photon loss. The average PMT rate for different dead times at −35 °C is shown in fig. 9.3. Evidently, the PMT rate decreases for increasing dead times since more photons are resolved as single pulses, mainly impacting Cherenkov photons. For each module developed for IceCube, certain requirements have to be fulfilled. Regarding the pulse pair resolution of PMTs for the mDOM, the system must be able to resolve individual pulses separated by 10 ns or more [63]. Hence, this value is chosen when simulating rates for different temperatures as shown in fig. 9.4. The temperature slope of PMT rates is solely determined by the temperature dependence of both scintillation yields combined while the dark rate is excluded.

The given rates look promisingly lower than anticipated from measurements, but unfortunately cannot be directly compared to one of a recently manufactured vessel at the time of writing. However, a measurement for the PMT background was done in a half vessel manufactured in 2015 [64].
For this, both scintillation yields have to be determined from samples of the 2015 manufacturing batch. In section 7.3 the electron yield was measured for both available batches, where the recent glass seems to incorporate less luminescent centres, given the lower yield. In section 8.2 however, the alpha yield could only be measured for the 2018 batch. To establish an approximate alpha yield for the 2015 glass, the ratio of yields from the 2018 batch is taken and applied to the electron yield for each temperature:

$$Y_{\alpha,2015}(T) \approx Y_{\mathrm{e},2015}(T) \cdot \frac{Y_{\alpha,2018}(T)}{Y_{\mathrm{e},2018}(T)}.$$

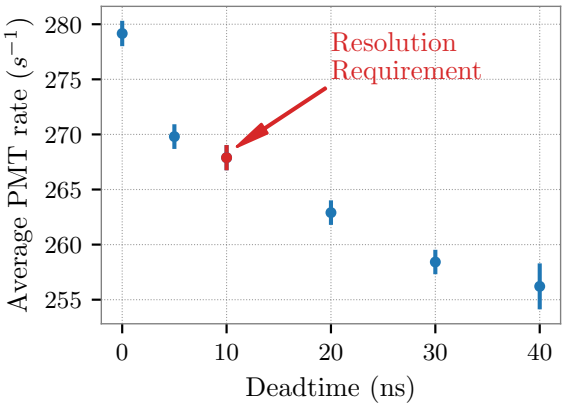

Fig. 9.3: Influence of individual PMT dead time on the average rate of photon detection. The uncertainties only regard the statistical error.

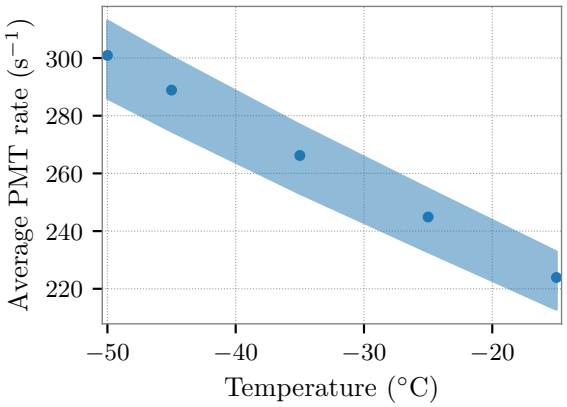

Fig. 9.4: Average PMT rate plotted against temperature. The asymmetric error stems from the uncertainty of the electron and alpha yield (see tables 7.3 and 8.3).

With both yields for the glass manufactured in 2015 and corresponding mDOM dimensions, the simulation is repeated for different temperatures. The dead time of the measurement is 5 ns which is consequently applied to the simulation as well. The comparison of both results is shown in fig. 9.5.

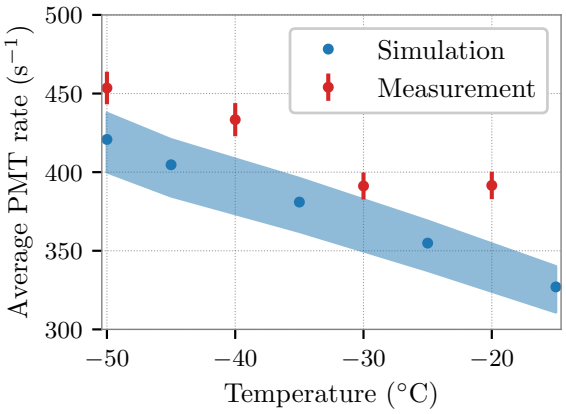

Fig. 9.5: Average PMT rate for mDOMs with glass vessels manufactured in 2015. The simulation (blue) considers the uncertainty stemming from both scintillation yields and the measurement (red) states the statistical error.

The expected PMT rates from the simulation seem to reflect the measurement quite well and shows that the modelled scintillation parameters are applicable. Furthermore, the measurement is not corrected for PMT dark rate (expected to be $\sim 25\,\mathrm{s}^{-1}$ at $-50\,°\mathrm{C}$) which would align the results even better.
However, when implementing a large dead time of 2.45 µs, the measurement shows a signal loss of $\sim 25\,\%$ in comparison to 5 ns, where the simulation exhibits a difference of about 51 %. This larger loss is due to the fact that the timing distribution of scintillation lifetime has more than three components. The measurement in [10] was done with waveforms of 100 µs and with this, all slower components are not measured. Thus a portion

of generated scintillation photons is emitted faster in the simulation than in reality. This causes faster photon arrival times which is subsequently cut off severely by dead times corresponding to the assumed lifetimes.

Comparing the expected background rate from both glass manufacturing batches (figs. 9.4 and 9.5), there is a 40-46 % decrease. This difference is solely linked to the determined scintillation yield caused by impurities and defects in the glass. Likewise, the amount of trace isotopes in the glass may also vary between manufacturing batches, which was not incorporated into the simulations due to the lack of measurements, whereas the influence of scintillation yields is emphasised here.
While this may lead to the assumption that more recently produced glasses result in lower module background rates, it genuinely conveys a spread between glasses. The difference in scintillation intensity stems from a higher concentration or different composition of the scintillating materials in the borosilicate glass, such as cerium. Between both manufacturing batches, the reservoir in which the compounds are melted in was exchanged, in which e.g. cerium is also contained. As of the time of writing it has not been investigated how and in which concentration traces from the reservoir contaminate the glass during the melting process. The extent is also reliant on the amount of glass, time of extraction, as well as age and material of the reservoir [63].

Nonetheless, the scintillation parameters determined in this work deliver satisfying results and pose an improvement to the previous description. The PMT rate of the measurement is reproduced more accurately due to the incorporation of both particle types causing scintillation.

10 Summary and outlook

This thesis aimed to progress the characterisation of scintillation parameters of the underlying module background as a follow up to [10]. The radioactive decays inside the Vitrovex pressure vessel of the mDOM, a new optical sensor which will be used in future IceCube extensions, represent the main background within the deep glacier ice which is almost free of optical activity. In this context, the proposed scintillation parameters were investigated in improved setups regarding different kinds of radioactive excitation.

Regarding the scintillation spectrum induced by α-particles, the data records the emission cut-off at $\sim (260.0 \pm 4.3)\,\mathrm{nm}$ due to the usage of UV-sensitive components. Furthermore, the contamination of air scintillation and transmission influences of the sample exhibited by the earlier measurement was removed. Thus, a more authentic spectrum is obtained. The simulations show a difference of approximately 21 % for the yield when interchanging the previous data set with the one measured in this thesis.
However, this measurement can still be improved since the wavelength resolution suffered from the low photon output. The most straight-forward improvement would be to use a single stronger alpha source with an activity of several hundred MBq for higher energy deposition as discussed in section 6.3. If the efficiency of the setup cannot be improved further, bandpass filters in front of the viewport could alternatively replace the monochromator (which only transmits collimated photons) to increase the amount of photons reaching the PMT.
Furthermore, the UV-sensitive PMT is limited to a gain of 10^6 at 900 V. A higher gain results in a more distinct separation between PMT pulses and electronic noise. Additionally, the trigger had to be set at -4.2 mV (mean amplitude at $\sim$-9 mV) as the PMT base could not be improved to conventional performance within a suitable time frame. Due to the low probability of multi-photon detection from scintillation light, such a high trigger results in severe signal loss with this already low amplitude setup.
Additionally, this property should be measured temperature dependant as well since the scintillation spectrum may differ from the room temperature measurement. With this, the corrections as done in section 6.3 as well as the absorption length of the sample need to be characterised temperature dependant. This would deliver more precise results for the scintillation yields since the room temperature spectrum is used for all simulations.
Lastly, scintillation photon emission is dependent on the type of excitation i.e. particle as shown by the measurements. This implies that the spectrum for electron excitation must be measured again, whereas photons generated by Cherenkov radiation must be suppressed to obtain the actual scintillation emission. An electron emitter (e.g. a compact electron gun) with $E_\mathrm{e} < 0.16\,\mathrm{MeV}$ with high intensity should be considered.

The scintillation yield by radioactive excitation was until now solely measured for alpha excitation whereas the electron yield was estimated by multiplication of factor 9.5. Due to δ- and ionisation electrons following alpha interactions, the electron yield must be determined first for realistic simulations. Comparing both obtained yields shows that the ratio is not simply scaled by a factor, but temperature dependant.

PMT effects such as trigger loss were considered before, but are now further corrected for afterpulsing loss which can impact the results by as much as 12 %.
One aspect that could be explored are the radioactive sources. One needs to verify whether all β^- decays of the ^{137}Cs source are captured by the shielding material. If these electrons were to excite the glass samples, it would result in an inflated yield since they were not simulated. Further, PMT signals caused by γ-particles could be investigated. As mentioned, they may stem from scintillation of the glass envelope, excitation of the photocathode or release of photoelectrons from gammas interacting with the dynodes.

Looking forward, individual modules or even entire IceCube background simulations due to scintillation light production can now be computed more accurately which in this case is as easy as inputting new parameters into the simulation framework.
The investigations in chapter 9 show that the expected PMT rates from the simulations are in good agreement with a measurement of a half vessel. This concludes, that the modelling of scintillation parameters in this thesis is factual and delivers more accurate results than before.

Lastly, the lifetime should additionally be measured for electron scintillation. Although it was estimated to be similar to scintillation induced by α-particles in section 7.4, it needs to be verified. On this note, the scintillation lifetime resulting from alphas should be measured with longer waveforms to capture every radiative transition.

It is to emphasise, that all investigations are valid for the composition of Vitrovex glass and as seen in fig. 7.22, the produced amount of scintillation light can even vary between manufacturing batches. The best assumption for this is that lattice defects and/or impurity atom are likely to vary between different samples and the scintillation yield is dependant on that. For this, a broader variety of production batches should be investigated for a better estimation of the spread which will be done during the production of mDOMs. Nonetheless, Vitrovex is the baseline brand for the assembly of mDOMs and the determined scintillation parameters should thus not deviate strongly from future productions.

Bibliography

[1] M. G. Aartsen, et al. (IceCube Collaboration), *First observation of PeV-energy neutrinos with IceCube*, Phys. Rev. Lett. 111, 021103 (2013) Preprint arXiv:1304.5356.

[2] M. G. Aartsen, et al. (IceCube Collaboration), *Evidence for high-energy extraterrestrial neutrinos at the IceCube detector*, Science 342, 1242856 (2013) Preprint arXiv:1311.5238.

[3] M. G. Aartsen, et al. (IceCube Collaboration), *Neutrino emission from the direction of the blazar TXS 0506+056 prior to the IceCube-170922A alert*, Science 361 (2018) 147–151. URL https://science.sciencemag.org/content/361/6398/147

[4] L. Classen, A. Kappes, T. Karg, *A multi-PMT Optical Module for the IceCube Upgrade* (2019). URL https://arxiv.org/abs/1908.10802

[5] A. Ishihara (IceCube Collaboration), *The IceCube Upgrade – Design and Science Goals* (2019). URL https://arxiv.org/abs/1908.09441

[6] M. G. Aartsen, et al. (IceCube Collaboration), *IceCube-Gen2: A Vision for the Future of Neutrino Astronomy in Antarctica*, PoS FRAPWS2016 (2017) 004, Preprint 1412.5106.

[7] T. Eder, *Simulationsstudien zum Untergrund durch radioaktive Zerfälle in einem optischen Modul mit mehreren Photomultipliern für IceCube-Gen2*, Bachelor Thesis, Westfälische Wilhelms-Universität Münster (2016). URL https://www.uni-muenster.de/imperia/md/content/physik_kp/agkappes/abschlussarbeiten/bachelorarbeiten/1609-ba_teder.pdf

[8] K. Helbing, et al., *Light emission in Amanda pressure spheres*, AMANDA-Internal report (2003).

[9] O. Franzen, *Untersuchungen optischer module für das AMANDA- bzw. IceCube-projekt*, Diplomarbeit, Johannes Gutenberg-Universität zu Mainz (2003).

[10] M. Unland, *Studies on dark rates induced by radioactive decays of the multi-PMT digital optical module for future IceCube extensions*, Master's thesis, Westfälische Wilhelms-Universität Münster (2017). URL https://www.uni-muenster.de/imperia/md/content/physik_kp/agkappes/abschlussarbeiten/masterarbeiten/1712-ma_munland.pdf

[11] Available at https://commons.wikimedia.org/wiki/File:Standard_Model_of_Elementary_Particles_modified_version.svg; last called on 16.09.2019. (2014).

[12] M. Aker, et al. (KATRIN Collaboration), *Improved Upper Limit on the Neutrino Mass from a Direct Kinematic Method by KATRIN*, 123 (22) (2019) 221802, Preprint 1909.06048. URL https://arxiv.org/abs/1909.06048

[13] B. T. Cleveland, et al., *Measurement of the Solar Electron Neutrino Flux with the Homestake Chlorine Detector*, The Astrophysical Journal 496 (1) (1998) 505–526. URL https://doi.org/10.1086%2F305343

[14] K. S. Hirata, et al., *Real-time, directional measurement of ^8B solar neutrinos in the Kamiokande II detector*, Physical Review D 44 (8) (1991) 2241–2260. URL https://doi.org/10.1103/physrevd.44.2241

[15] C. Spiering, *Towards high-energy neutrino astronomy*, The European Physical Journal H 37 (3) (2012) 515–565. URL https://doi.org/10.1140/epjh/e2012-30014-2

[16] T. K. Gaisser, R. Engel, E. Resconi, Cosmic Rays and Particle Physics, 2nd Edition, Cambridge University Press, 2016. URL https://doi.org/10.1017/CBO9781139192194

[17] U. F. Katz, C. Spiering, *High-Energy Neutrino Astrophysics: Status and Perspectives*, Prog. Part. Nucl. Phys. 67 (2012) 651–704, Preprint 1111.0507.

[18] L. Classen, *The mDOM - a multi-PMT digital optical module for the IceCube-Gen2 neutrino telescope*, PhD thesis, Friedrich-Alexander-Universität Erlangen-Nürnberg (2017). URL https://www.uni-muenster.de/imperia/md/content/physik_kp/agkappes/abschlussarbeiten/doktorarbeiten/1702-phd_lclassen.pdf

[19] M. G. Aartsen, et al. (IceCube Collaboration), *The IceCube Neutrino Observatory: Instrumentation and Online Systems*, JINST 12 (03) (2017) P03012, Preprint 1612.05093.

[20] C. Fruck, F. Henningsen, C. Spannfellner, *The POCAM as self-calibrating light source for the IceCube Upgrade* (2019). URL https://arxiv.org/abs/1908.09600

[21] Photomultiplier tubes - Basics and Applications, 3rd Edition, Hamamatsu Photonics K.K., 2007. URL https://www.hamamatsu.com/resources/pdf/etd/PMT_handbook_v3aE.pdf

[22] Photomultiplier tubes - Photomultiplier tubes and related products, Hamamatsu Photonics K.K. URL https://www.hamamatsu.com/resources/pdf/etd/PMT_TPMZ0002E.pdf

[23] M. Suyama, K. Nakamura, Recent Progress of Photocathodes for PMTs, Proceedings of science, 2009. URL https://pos.sissa.it/090/013/pdf

[24] S.-O. Flyckt, C. Marmonier, Photomultiplier tubes - Principles and applications, Photonis, 2002. URL http://www2.pv.infn.it/~debari/doc/Flyckt_Marmonier.pdf

[25] M. Unland, L. Classen, J. Reubelt, S. Schmiemann, J. Schneider, A. Kappes, *Characterisation of the Hamamatsu R12199-01 HA MOD photomultiplier tube for low temperature applications*, Journal of Instrumentation 14 (2019). URL https://doi.org/10.1088/1748-0221/14/03/p03015

[26] M. Dittmer, *Charakterisierung von Photomultipliern mit hoher Quanteneffizienz vom Typ Hamamatsu R12199 HQE*, Master's thesis, Westfälische Wilhelms-Universität Münster (2017). URL https://www.uni-muenster.de/imperia/md/content/physik_kp/agkappes/abschlussarbeiten/bachelorarbeiten/1710-ba_mdittmer.pdf

[27] T. Wright, A. Wright, The Photomultiplier Handbook, Oxford University Press, 2017, ISBN: 9780199565092.

[28] E. H. Bellamy, et al., *Absolute calibration and monitoring of a spectrometric channel using a photomultiplier*, Nuclear Instruments and Methods in Physics Research A 339 (1994) 468–476. URL https://doi.org/10.1016/0168-9002(94)90183-X

[29] K. W. Fornalski, *Simple empirical correction functions to cross sections of the photoelectric effect, compton scattering, pair and triplet production for carbon radiation shields for intermediate and high photon energies*, Journal of Physics Communications 2 (3) (2018) 035038. URL https://doi.org/10.1088%2F2399-6528%2Faab408

[30] W. Frass, *Passage of particles through matter*, (2009). URL https://www2.physics.ox.ac.uk/sites/default/files/Passage.pdf

[31] O. Boyarkin, Advanced Particle Physics - Particles, Fields, and Quantum Electrodynamics, CRC Press, Boca Raton, Fla, 2011, ISBN: 978-1-439-80414-8.

[32] F. Helus, Radionuclides Production, CRC Press, 1993, ISBN: 978-1-000-01317-7.

[33] Berger, et al., *XCOM: Photon cross sections database - NIST standard reference database 8 (XGAM)*, NIST, PML, Radiation Physics Division, available at https://dx.doi.org/10.18434/T48G6X; last called on 12.09.2019. (2010).

[34] M. Berger, J. Coursey, M. Zucker, J. Chang, *Stopping-Power & Range Tables for Electrons, Protons, and Helium Ions - NIST Standard Reference Database 124*, NIST, PML, available at https://dx.doi.org/10.18434/T4NC7P; last called on 12.09.2019. (2017).

[35] F. Bloch, *Zur Bremsung rasch bewegter Teilchen beim Durchgang durch Materie*, Annalen der Physik 408 (3) (1933) 285–320. URL https://doi.org/10.1002/andp.19334080303

[36] H. Bichsel, *Barkas effect and effective charge in the theory of stopping power*, Physical Review A 41 (7) (1990) 3642–3647. URL https://doi.org/10.1103/physreva.41.3642

[37] M. J. Berger, et al., *Report 49*, Journal of the International Commission on Radiation Units and Measurements os25 (2) (1993) NP–NP. URL https://doi.org/10.1093/jicru/os25.2.report49

[38] H. Bichsel, *Stopping power of fast charged particles in heavy elements* (1991). URL https://nvlpubs.nist.gov/nistpubs/Legacy/IR/nistir4550.pdf

[39] J. C. Ashley, R. H. Ritchie, W. Brandt, Z_1^3 *effect in the stopping power of matter for charged particles*, Phys. Rev. B 5 (1972) 2393–2397. URL https://link.aps.org/doi/10.1103/PhysRevB.5.2393

[40] J. C. Ashley, R. H. Ritchie, W. Brandt, Z_1^3*-dependent stopping power and range contributions*, Phys. Rev. A 8 (1973) 2402–2408. URL https://link.aps.org/doi/10.1103/PhysRevA.8.2402

[41] H. Andersen, J. Ziegler, *Hydrogen stopping powers and ranges in all elements.*, Pergamon Press (1977) ISBN: 978-0080216058.

[42] J. F. Ziegler, Helium: stopping powers and ranges in all elemental matter, Pergamon Press New York, 1977, ISBN: 978-0080216065.

[43] C. Varelas, J. Biersack, *Reflection of energetic particles from atomic or ionic chains in single crystals*, Nuclear Instruments and Methods 79 (2) (1970) 213–218. URL https://doi.org/10.1016/0029-554x(70)90141-2

[44] H. Bethe, *Zur Theorie des Durchgangs schneller Korpuskularstrahlen durch Materie*, Annalen der Physik 397 (3) (1930) 325–400. URL https://doi.org/10.1002/andp.19303970303

[45] H. Bethe, *Bremsformel für Elektronen relativistischer Geschwindigkeit*, Zeitschrift für Physik 76 (5-6) (1932) 293–299. URL https://doi.org/10.1007/bf01342532

[46] CERN, *CERN Yellow Reports: School Proceedings, Vol 2 (2017): Proceedings of the 2014 Asia-Europe-Pacific School of High-Energy Physics* (2017). URL https://e-publishing.cern.ch/index.php/CYRSP/issue/view/38

[47] I. M. Tsidilkovski, Electron Spectrum of Gapless Semiconductors, Springer Berlin Heidelberg, 1997. URL https://doi.org/10.1007/978-3-642-60403-4

[48] B. G. Yacobi, D. B. Holt, Cathodoluminescence Microscopy of Inorganic Solids, Springer US, 1990. URL https://doi.org/10.1007/978-1-4757-9595-0

[49] R. Salh, *Defect Related Luminescence in Silicon Dioxide Network: A Review*, in: Crystalline Silicon - Properties and Uses, InTech, 2011, DOI: 10.5772/22607.

[50] C. Ronda, *Emission and excitation mechanisms of phosphors*, Luminescence: From Theory to Applications (2007) 1–34. URL https://onlinelibrary.wiley.com/doi/abs/10.1002/9783527621064.ch1

[51] J. I. Pankove (Ed.), Electroluminescence, Springer Berlin Heidelberg, 1977, DOI: 10.1007/3-540-08127-5.

[52] K. N. Shinde, S. J. Dhoble, H. C. Swart, K. Park, Basic Mechanisms of Photoluminescence, Springer Berlin Heidelberg, Berlin, Heidelberg, 2012, pp. 41–59. URL https://doi.org/10.1007/978-3-642-34312-4_2

[53] E. Kuwana, E. M. Sevick-Muraca, *Fluorescence lifetime spectroscopy in multiply scattering media with dyes exhibiting multiexponential decay kinetics*, Biophysical Journal 83 (2) (2002) 1165–1176. URL https://doi.org/10.1016/s0006-3495(02)75240-5

[54] J. B. Birks, The Theory and Practice of Scintillation Counting, Pergomon press, 1964. URL https://doi.org/10.1016/c2013-0-01791-4

[55] J. Allison, et al., *Recent developments in Geant4*, Nuclear Instruments and Methods in Physics Research Section A: Accelerators, Spectrometers, Detectors and Associated Equipment 835 (2016) 186–225. URL https://doi.org/10.1016/j.nima.2016.06.125

[56] A. Obermeier, *The fluorescence yield of air excited by electrons measured with the AIRFLY experiment*, Ph.D. thesis, Karlsruhe U. (2007). URL https://publikationen.bibliothek.kit.edu/200067269

[57] J. Rademacker, *An exact formula to describe the amplification process in a photomultiplier tube*, Nuclear Instruments and Methods in Physics Research Section A: Accelerators, Spectrometers, Detectors and Associated Equipment 484 (1-3) (2002) 432–443. URL https://doi.org/10.1016/s0168-9002(01)02055-1

[58] PHYWE SYSTEME GMBH Co. KG, *Study of the α-energies of ^{226}Ra with MCA*, available at https://www.techno-sciences.fr/wp-content/uploads/2017/08/p2522315.pdf; last called on 17.04.2020.

[59] G. Lefeuvre, P. Gorodetzky, J. Dolbeau, T. Patzak, P. Salin, *Absolute measurement of the nitrogen fluorescence yield in air between 300 and 430 nm* Preprint arXiv:0704.1532.

[60] C. Thompson, E. Barritt, C. Shenton-Taylor, *Predicting the air fluorescence yield of radioactive sources*, Radiation Measurements 88 (2016) 48–54. URL https://doi.org/10.1016/j.radmeas.2016.02.013

[61] J. Sand, et al., *Radioluminescence yield of alpha particles in air*, New Journal of Physics 16 (5) (2014) 053022. URL https://iopscience.iop.org/article/10.1088/1367-2630/16/5/053022

[62] F. de Chaffaut, *The luminescence decay time of air and nitrogen-oxygen mixtures excited by alpha particles*, IEEE Transactions on Nuclear Science 19 (3) (1972) 112–118. URL https://doi.org/10.1109/tns.1972.4326710

[63] A. Kappes, private communication.

[64] M. Unland, private communication.

Acknowledgements

I am very thankful to my advisor Prof. Alexander Kappes for giving me the opportunity to be a part of his splendid working group once again. Thank you for your guidance, support and patience, as well as the possibility for the continuation regarding this fascinating topic. You – as the *'boss'* of this group – create a very friendly and encouraging environment.
In that sense, I would also like to thank my second supervisor Dr. Volker Hannen for once more taking his time to evaluate this thesis.

My deepest gratitude has to go to Martin Unland who will probably find this part cringe-worthy. Ever since I was a little bachelor you tought me everything I know (and already forgot), even if you had to repeat yourself and explain basic stuff to me all over again. I am not able to put into words how much you contributed to my development in the past few years. Seriously man, thank you for everything.
Additionally, I want to take the opportunity to also praise Dr. Lew Classen and Chris Lozano in this regard for their availability for my questions if – or rather when – I got stuck somehow.
Furthermore, I want to thank the whole AG Kappes working group, not only for their support, but moreover for the continuously pleasant mood which has greatly motivated me to be productive and feel well during the time of my stay. You are truly awesome people to the extent that I regard each and everyone of you as a close friend of mine.
This entire experience made the last few years to the best times of my studies by a long shot and I cherished each moment. To be honest, I sincerely hope that this goodbye does not result in a departure forever..

There are many more people within the institute apart from the internal working group that helped me in the course of this journey. Thus, I would like to express my gratitude to Prof. Alfons Khoukaz, Prof. Klein Bösing, Hans-Werner Ortjohan, Christian Huhmann, Lutz Althüser, Roland Berendes and Tristan Böhm.

Honorable mentions go out to everyone that took their valuable time to proofread this mess and contributed to (hopefully) get rid of all mistakez. Shout-out to y'all!

And lastly, I want to seize the moment to thank my parents Gerhard and Regina Dittmer whom I owe more to than anybody else in this world. Your never ending support was the foundation for me to finish my entire path of education as of yet. Apart from the reason that you gave everything in your means to raise me to your best extent, I am thankful that you were always by my side even in less charming times. I would (literally) not be where I am today if it wasn't for the two of you.